RESEARCH ARTICLE

Estimation of future extreme rainfall in Barcelona (Spain) under monofractal hypothesis

Robert Monjo[1,2] | **Luca Locatelli**[3] | **John Milligan**[3] | **Luis Torres**[1] | **Marc Velasco**[3] | **Emma Gaitán**[1] | **Javier Pórtoles**[1] | **Darío Redolat**[1] | **Beniamino Russo**[3,4] | **Jaime Ribalaygua**[1]

[1]Climate Research Foundation – Fundación para la Investigación del Clima (FIC), Madrid, Spain

[2]Department of Algebra, Geometry and Topology, Complutense University of Madrid (UCM), Madrid, Spain

[3]AQUATEC (AGBAR Group), Zona Franca Avenue, 46-48, Barcelona 08038, Spain

[4]Flumen Research Institute, Universitat Politècnica de Catalunya - BarcelonaTech (UPC), Campus Nord, Jordi Girona 1-3, 08034 Barcelona, Spain

Correspondence
Robert Monjo, Climate Research Foundation – Fundación para la Investigación del Clima (FIC), Madrid, Spain.
Email: robert@ficlima.org

Funding information
European Commission, Grant/Award Numbers: 101093806, 700174; MITECO

Abstract

Climate change effects on subdaily rainfall (from 5 min to a few hours) can hardly be measured in mid-latitude climates due to the high natural variability of the precipitation patterns and their effects on local topography. The goal of this study was to obtain change projections of intensity–duration–frequency (IDF) curves, for up to 2-h precipitation events, comparing two approaches that use the daily outputs of the downscaled Coupled Model Intercomparison Project Phase 5 (CMIP5) multi-model projections: (a) direct scaling of the expected probable precipitation, from 2-year to 500-year return periods of daily rainfall and (b) a new semi-stochastic approach, built by combining the physically forced outputs of climate models (on a daily scale) and stochastic simulation given by the probability distribution of a concentration index (n-index) for individual rainfall events (on a subdaily scale). The approaches were applied to a set of 27 stations located around Barcelona, Spain, including a long reference series (with 5-min rainfall records since 1927), representing the highly variable Mediterranean climate. The validation process showed a systematic error (bias) generally smaller than 10%, especially for rainfall extreme events with durations of less than 2 h. The concentration n-index and IDF curves were projected by 10 downscaled CMIP5 climate models under 2 emission scenarios (RCP4.5 and RCP8.5), obtaining a consensual increase in both relative concentration and absolute intensities in Barcelona. Ensemble projection of rainfall concentration (n-index) showed an increase up to 10% by 2071–2100 and about 20% (15%–30% range) for maximum intensities of 2-year to 500-year return periods. Results provide robustness in decision-making regarding the design of stormwater management infrastructure at a local scale.

KEYWORDS
concentration index, downscaling, extreme rainfall, monofractal, subdaily rainfall

1 | INTRODUCTION

1.1 | Motivation

Rainfall presents self-similarity in several time scales, which is a geometric property known as *fractality* (due to chaotic dynamical systems). This implies that rainfall intensity has a geometric dimension that is neither punctual (dimension = 0) nor linear (dimension = 1) but fractional (between 0 and 1) that may or may not depend on the time scale. When dimension depends on the time-scale, it is known as multifractal, while a weak temporal dependency is assumed under the monofractal hypothesis. This study tested the performance of the simple scaling approach (*monofractal hypothesis*) to describe the behaviour of point extreme rainfall in the *intensity–duration–frequency* (IDF) relationship at a local scale. A double method was designed to obtain consensual results for subdaily rainfall, which is significant because its extreme events present stratiform and convective origin features, that is, with different temporal-dimension behaviours. Finally, this work also aimed to connect four different perspectives of the fractal dimension related to the power law of rainfall intensities: (a) IDF curves, (b) hyetograph in synthetic design storms, (c) rainfall concentration within a real event and (d) daily-to-subdaily rainfall disaggregation, detailed below.

1.2 | State of the art

1.2.1 | Climate modelling of rainfall

Global extreme precipitation (e.g., annual maximum daily precipitation) experienced a statistically significant increase due to global warming at a rate of between 5.9% and 7.7% K^{-1} in average (1900–2009 period), depending on the method of analysis (Westra et al., 2013). According to the Clausius–Clapeyron relation, atmospheric water content increases at about 6.8% K^{-1}, but the climate change signal in subdaily rainfall can be very different due to regional weather patterns, mesoscale processes and local convection (Barbero et al., 2017; Hardwick-Jones et al., 2010; Westra et al., 2013). Regarding precipitation in Europe, climate change scenarios are strongly conditioned by regional/local geographical features that should be considered using dynamical or statistical downscaling methods (Gutiérrez et al., 2019; Ribalaygua et al., 2013). Currently, regional and local climate scenarios are available from the downscaled outputs of the Coupled Model Intercomparison Project Phase 5 (CMIP5), with international initiatives such as CORDEX (Jacob et al., 2014) and European projects such as RESilience to

cope with Climate Change in Urban arEas (RESCCUE), among others (Velasco et al., 2018). In this context, dynamical models have an advantage over statistical methods regarding the spatial distribution and parameterization of convective processes on subdaily timescales (Chan et al., 2014; Meredith et al., 2019). However, biases in rainfall probability distribution of dynamical model outputs need to be corrected (with statistical methods) to analyse extreme precipitation, and therefore the dynamical and statistical approaches are complementary (Monjo et al., 2014, 2016).

Statistical approaches to spatial downscaling provide climate change scenarios on a daily timescale, and then a temporal downscaling (or time scaling) is required to obtain future regimes of subdaily rainfall, including extreme events. Expected maximum precipitation for a return period and on a subdaily duration is described using IDF curves, which are useful to create the well-known 'design storms' through synthetic hyetograph methods (Casas-Castillo et al., 2018a).

IDF curves are estimated based on empirical cumulative distribution functions (ECDFs) of annual maximum precipitation (at several time intervals) from peaks over thresholds or using the entire time series. They can be simulated by fitting theoretical distributions (i.e., parametric probability models). The most common functions to model the frequency term of the IDF curves are the Gumbel distribution, Weibull distribution, and the generalized extreme value (GEV), which are also used in temporal downscaling procedures (Monjo et al., 2016; Nguyen et al., 2007; Yeo et al., 2021).

1.2.2 | Rainfall disaggregation

Synthetic hyetographs are key in the modelling of subdaily rainfall events. Most classical approaches are based on observed cumulative curves, such as the alternating block technique, the Huff's quantiles (Huff, 1967), the Pilgrim–Cordery curves (Cordery & Pilgrim, 1984), and the Soil Conservation Service/Natural Resource Conservation Service (SCS/NRCS) Type I, II and III curves (Mishra et al., 2018). Other semi-empirical methods fit some smooth curves (e.g., Gaussian or Gamma distribution) akin to the Huang (2011) approach, using triangles as in the Yen–Chow method, or piecewise functions such as the Sifalda storm and the Keifer–Chu curves (or Chicago method), among others (Na & Yoo, 2018).

From a more theoretical viewpoint, synthetic hyetographs can also be obtained from stochastic processes of rainfall disaggregation. For instance, the method of fragments is a daily-to-subdaily scaling that uses a nonparametric resampling approach and conditional probability

distribution functions to relate daily rainfall vectors and the corresponding subdaily fragments from at-site records or other stations such as neighbouring or more correlated ones (Li et al., 2018; Rafatnejad et al., 2022).

Weather generators based on multi-state Markov chains are commonly used to concatenate wet/dry values of a synthetic time series (Peleg et al., 2017; Rayner et al., 2016). Convective features of rainfall can also be simulated by stochastic approaches, considering synthetic power law spectrums in filtered autoregressive models such as the RainFARM method (D'Onofrio et al., 2014) or using cumulative functions for extreme simulations as in the Stochastorm technique (Wilcox et al., 2021).

1.2.3 | Multifractal cascade approach

Random cascade models provide many ways to time-scaling rainfall, although they were developed originally for turbulence studies (Mandelbrot, 1974; Müller-Thomy, 2020). Sun and Barros (2010) used universal multifractal parameters to simulate rainfall time series according to several values of the Levy index, which indicates the deviation from the monofractal case. Multiplicative cascade models, such as the micro-canonical cascade processes, are also used to analyse the time-scaling of precipitation (Gaume et al., 2007; Müller-Thomy, 2020). However, Gao et al. (2018) used standard normal spaces from a log-ratio transformation of the intensities.

According to the probability distribution of multifractal fields (e.g., the rainfall intensity), the average of the statistical q-moment of the field is proportional to the power of the ratio or fraction of the scales involved (Garcia-Marin et al., 2013; Schertzer & Lovejoy, 1987; Zhang et al., 2021). Therefore, for scaling a synthetic rainfall event from t_0 to t duration, that is

$$\langle I_q(t) \rangle \sim \langle I_q(t_0) \rangle \left(\frac{t_0}{t} \right)^{\zeta(q)} \qquad (1)$$

where the operator $< \cdot >$ indicates average, $I_q(t_0)$ and $I_q(t_0)$ are the q-moments of the field for the timescales $t < t_0$, and $\zeta(q)$ is the scaling moment function (multifractal spectrum), which is from the Legendre transformation of the codimension function for the field considered (Masugi & Takuma, 2007; Sun & Barros, 2010). If the monofractal hypothesis is assumed for intensity or velocity fields, an asymptotic power law is found:

$$\zeta(q) \approx \check{n}q \qquad (2)$$

where $0 \leq \check{n} \leq 1$ is the simple scaling parameter or simple-scale cascading dimension that, for averaged

rainfall intensities, is approximately equivalent to the Lipschitz–Hölder exponent and the monofractal Rényi dimension (see Appendix A). Under a purely geometric viewpoint, it is the Minkowski–Bouligand box-counting dimension, which is the upper limit for the Hausdorff dimension (Bäcker et al., 2019; Metzler & Klafter, 2000; Schmitt & Huang, 2016).

1.2.4 | Approximation of the monofractal dimension by a concentration n-index

Applying the extreme value theory to the ($q = 1$)-moment (i.e., average) of the maximum probable intensity $I(T, t)$ for a return period T, Equation (1) is separable into two functions (h and λ), representing the dependency with the return period T and with the duration t (Casas-Castillo et al., 2018a, 2018b):

$$I(T,t) := h(T)\lambda(t) := h(T)\langle I_1(t) \rangle \qquad (3)$$

and the linked precipitation is directly $P(T, t) = I(\mathrm{T}, t) \cdot t$. Coherently with the theoretical approach of monofractal or simple scaling, the dependency function $\lambda(t)$ over the duration t was empirically modelled by many authors using a constant exponent (Casas-Castillo et al., 2018b; Yu et al., 2004). The most employed versions were introduced (still no fractal interpretation) by Sherman (1931) and Chow (1962), respectively.

$$f(t) = \frac{a}{(t+b)^{\check{n}}} \qquad (4)$$

$$f(t) = \frac{a}{t^{\check{n}}+b} \qquad (5)$$

where a, b and $\check{n}$ are fitting parameters. For real hyetographs (and not necessarily extreme events), approximating $b \sim 0$, the parameter $\check{n}$ is comparable to an index which describes how concentrated the rainfall is within an event (Moncho et al., 2009; Monjo, 2016), named n-index. The n-index is an approximation to the monofractal dimension ($\check{n}$) for the case of the order of moments $q = 1$ (Equation 2 and Appendix A), applied to observed hyetographs (corresponding to a wet spell, and no necessarily extreme). In this case, maximum averaged intensity (I) varies over duration (t) according to a power law,

$$I(t) = I_0 \left(\frac{t_0}{t} \right)^n \qquad (6)$$

where $0 \leq n \leq 1$ is the fitted value for the n-index and I_0 is the *reference intensity*, fitted for a given t_0 (e.g., 5 min).
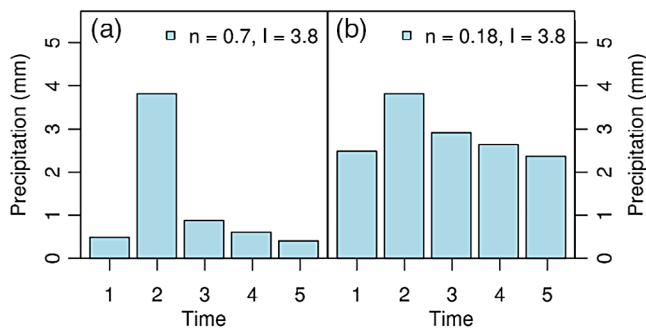
FIGURE 1 Example of same-duration hyetographs with similar maximum intensity but for different concentrations of rainfall according to the n-index: (a) high concentrated rainfall ($n = 0.7$) and (b) more uniform rainfall ($n = 0.18$). [Colour figure can be viewed at wileyonlinelibrary.com]

For each rainfall event (i.e., wet spell with at least three consecutive nonzero values), a value of the n-index can be obtained by sorting and then fitting the maximum averaged intensities as a function of durations ranged between the minimum t_0 and the total event duration d. This method can be applied for a large set of timescales and durations (from a few minutes to supradaily scales), resulting different ranges of values of n, even for the same location. Particularly, Monjo et al. (2016) found that, for two different time resolutions (r_1 and r_2) between 1 and 12 h, the corresponding n-index (n_1 and n_2) varies as $\Delta n = n_2 - n_1 \approx k \cdot \ln(r_2/r_1)$, where $k = 0.028 \pm 0.003$ was fitted for individual rainfall events of 5347 subdaily time series around the world (with n_1 typically ranged between 0.2 and 0.8).

Under the monofractal hypothesis, the value of n is assumed to be approximately independent of the duration and time resolution. In this case, it represents the relative concentration linked to the time structure of convective-stratiform processes (Figure 1). For instance, on the hourly scale, rainfall with mostly stratiform origin (i.e., with predominant advection) usually shows low n-index values ($n < 0.4$), while mesoscale convective systems (i.e., convection fed by organized warm-wet advection) present values of about 0.4–0.6, and purely convective systems (mostly vertical flows) are characterized by a fast evolution and short life cycle with $n > 0.6$ (Moncho et al., 2009, 2011; Monjo, 2016). In contrast, on a daily scale and calculated from annual maximum rainfall series, values of the fractal-related parameter ($\check{n}$) are usually greater than 0.7 (Bara et al., 2010; Casas-Castillo et al., 2018b).

Notice that Equation (6) is the same as Equation (1) with Equation (2) for the statistical one-moment (average). The n-index is very close to the monofractal dimension of rainfall obtained, for example, from box-counting

and provides information about its more or less convective nature (Meseguer-Ruiz et al., 2019; Monjo, 2016; Monjo & Martin-Vide, 2016).

Methods based on fractal (chaotic) properties of rainfall are also suitable to model subdaily extreme rainfall for Mediterranean climates (Ghanmi et al., 2013; Rodríguez-Solà et al., 2017). The power law (Equations 4 and 5 with $b \sim 0$) is commonly used as an envelope curve to estimate the values of Probable Maximum Precipitation for the entire time series (Casas-Castillo et al., 2018a, 2018b; Galmarini et al., 2004; Gonzalez & Bech, 2017; Moncho et al., 2011). However, self-similarity properties of the fractal-based nature provide not only scaling of maximum intensities for all timescales of the rainfall but also modelling of wet/dry spells and drought lacunarity (Monjo, 2016; Monjo et al., 2020).

To test time-scaling methods, the Jardí gauge of the Fabra Observatory of Barcelona (Spain) can be considered a standard reference because of the high time resolution (5-min data since 1927) and many previous studies performed using the Fabra time series (Llasat, 2001; Rodríguez-Solà et al., 2017). For instance, Burgueño et al. (1994) carried out the digitalization of the paper rolls recorded by the pluviograph and its calibration to obtain statistics of hourly rainfall. Earlier, Puigcerver et al. (1986) analysed the maximum rain rates for Barcelona, and then Llasat and Puigcerver (1997) studied the convective ratio of rainfall in the region. Casas et al. (2011) combined physical and statistical methods to obtain maximum precipitation expected. Rodríguez et al. (2013, 2014) analysed multifractal parameters for local rainfall under different synoptic configurations and estimated the effects of climate change on the IDF curves in Barcelona. More recently, Rodríguez-Solà et al. (2017) focused on the time-scaling properties of rainfall to generate IDF curves from Spanish daily records, including the Fabra Observatory.

1.2.5 | Objectives of the study

In the context of climate change modelling, this study aims to analyse the monofractal features of subdaily rainfall to compare two methods of obtaining IDF curves from climate models, downscaled to Barcelona with a daily time resolution. The first method calculates the climate change factors (CCFs) according to Arnbjerg-Nielsen (2012), combining the monofractal downscaling method (Rodríguez-Solà et al., 2017) and statistical extreme value analyses. The CCF compares future projections and historical experiments of climate models, and it is expressed as a 'multiplicative factor', applied to the historical IDF curves to obtain new ones. The second
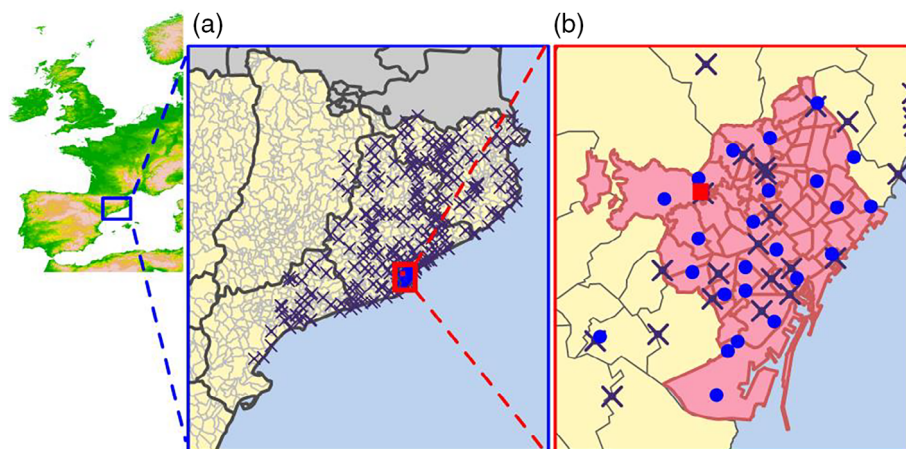
FIGURE 2 Location of the stations used in this study: (a) set of 300 high-quality stations (75% of records in the 1980–2021 period) located in Ter-Llobregat System (Catalonia, Spain) with daily records of precipitation (AEMET) and (b) network of subdaily recording from 27 stations (90% of records in the same period) located in the Barcelona area for precipitation (BCASA). The Jardí gauge of Fabra Observatory (Royal Academy of Sciences and Arts of Barcelona) is highlighted with a small square within the city of Barcelona (red shadow area). [Colour figure can be viewed at wileyonlinelibrary.com]

method leads to the generation of a semi-stochastic sub-daily time series, using several properties of the point-rainfall data (i.e., measured in a rain gauge), combining daily physical forcing and the (stochastic) probability distribution of the concentration n-index for the individual rainfall events. As a novelty, this work obtains and analyzes projected changes of the concentration n-index throughout the 21st century, used as an approximation of the *simple-scaling exponent* or *monofractal parameter* ($\check{n}$).

2 | STUDY AREA AND DATA

2.1 | Observation data

As statistical methodologies try to simulate point observations by using their records, geographical coherence and granularity depend on the density and spatial distribution of the used reference stations. In this study, projections of extreme rainfall could be spatially analysed because of the subdaily time series of 27 observatories located around Barcelona (Catalonia, Northern Spain) and, to support the spatial interpolation, also 300 time series with daily rain gauges (Figure 2) distributed throughout the Ter-Llobregat hydrological system, which corresponds to Barcelona. The time series of daily data (with at least 75% of the records in the 1980–2021 period) was provided by the Spanish State Meteorology Agency (AEMET, Spanish acronym), while subdaily precipitation (with at least 90% of records in the same period) was collected from the Barcelona Cicle de l'Aigua S.A. (BCASA).

Barcelona is an example of a climate change hotspot within the Mediterranean region, with high natural variability in extreme climate events impacting the water systems (Monjo et al., 2016; Rodríguez et al., 2014; Velasco et al., 2018). It has a hot dry-summer climate (Csa according to the Köppen climate classification), with an annual rainfall that varies between 300 and 1000 mm, especially depending on the Western Mediterranean Oscillation phases (Bonsoms et al., 2021; Martin-Vide & Lopez-Bustins, 2006). The highest efficiency in rainfall is recorded generally during autumn, related to heavy precipitation events caused by organized (mesoscale) convective systems embedded in synoptic formations (Casas et al., 2011; Gonzalez & Bech, 2017). The physical features of its extreme rainfall events combine fast currents (typically convective upward and downward flows) and slow streams derived by advective flows from the Mediterranean Sea, which provide a higher efficiency in the moisture feeding to storms. This phenomenon is known as mixed (convective-stratiform) rainfall (Llasat, 2001), and it can also be modelled by the monofractal dimension (Monjo, 2016; Monjo et al., 2020).

To deeply analyse the temporal behaviour of the rainfall projections, this work was especially focused on its most commonly used station for climate analysis of subdaily precipitation in Spain, namely the Jardí gauge of Fabra Observatory of the Royal Academy of Sciences and Arts of Barcelona, with collaborations with the Spanish and Catalan meteorological agencies. This observatory is a remarkable reference for other time series of subdaily rainfall because it has provided 5-min resolution records since June 1927, with only one gap

TABLE 1 Available CMIP5 climate models with outputs on a daily timescale. The table shows the responsible institution, climate model version, respective references and spatial resolution for the AGCM and the OGCM. The case of $lon(i,j) \times lat(i,j)$ denotes longitudes and latitudes depending on each grid point (represented as indices i and j).

Institution	CMIP5 model	References	AGCM resolution (Lon × Lat)	OGCM resolution (Lon × Lat)
CSIRO, BOM	ACCESS1-0	Bi et al. (2013)	1.87° × 1.25°	$lon(i,j) \times lat(i,j)$
BCC	BCC-CSM1-1	Xiao-Ge et al. (2013)	2.8° × 2.8°	1.0° × 0.33°
CC-CMA	CanESM2	Chylek et al. (2011)	2.8° × 2.8°	1.41° × 0.93°
CNRM-CERFACS	CNRM-CM5	Voldoire et al. (2013)	1.4° × 1.4°	$lon(i,j) \times lat(i,j)$
GFDL	GFDL-ESM2M	Dunne et al. (2012)	2° × 2.5°	1.0° × 0.33°
MOHC	HADGEM2-CC	Collins et al. (2008)	1.87° × 1.25°	1.0° × 0.33°; 1.25° × 0.25°
JAMSTEC, AORI, NIES	MIROC-ESM-CHEM	Watanabe et al. (2011)	2.8° × 2.8°; 1.4° × 1.4°	1.7° × 0.56°; 0.5° × 0.5°
MPI-M	MPI-ESM-MR	Marsland et al. (2003)	1.8° × 1.8°	$lon(i,j) \times lat(i,j)$
MRI	MRI-CGCM3	Yukimoto et al. (2011)	1.2° × 1.2°	1.0° × 0.5°
NCC	NorESM1-M	Iversen et al. (2012)	2.5° × 1.9°	$lon(i,j) \times lat(i,j)$

between October 1992 and July 2008. That is, the time series contains more than 8 million 5-min rainfall records up to 2021. The gap was filled by 5-min data available in the closest station, applying a quantile-mapping adjusted from the common period with Jardí Fabra (specifically, we used a parametric approach described in Monjo et al., 2016). Throughout the manuscript, we refer to these data as *observed data*.

Several tests were applied to all the observed time series for quality control, including general consistency (e.g., possible false zeros, accumulation in 2 days, etc.). In particular, outliers/inhomogeneity analysis based on the Kolmogorov–Smirnov (KS) test was performed following the protocol developed by Monjo et al. (2013).

2.2 | Climate model data

Atmospheric variables were collected from the ERA-Interim reanalysis and 10 CMIP5 model outputs for both historical experiments (1951–2005) and future projections (2006–2100) (Table 1). Atmospheric fields (specific humidity at 700 hPa and wind speed and direction for both 1000 and 500 hPa) were selected as predictor variables in a statistical downscaling method (see Section 3.2). For the climate projections, the Representative Concentration Pathways 4.5 and 8.5 (RCP4.5 and RCP8.5) were considered. The raw run, r1i1p1, was taken for all climate models except for CanESM2, for which the r2i1p1 run was available. They consist of the complete forcing

conditions (i1p1) applied to the available run in each case (r1 or r2).

3 | METHODOLOGY

3.1 | General scheme of methodologies used and their motivation

This work applied a statistical spatial downscaling to CMIP5 model outputs (Table 1) to obtain daily time series at a local scale (Section 3.2), combined with two different approaches for scaling the time resolution from the day to the 5-min detail in IDF curves. For this purpose, a simple scaling is directly applied to the past extreme events with low computational cost (Section 3.3) and, on the other hand, a sophisticated semi-stochastic technique is proposed to obtain future projections of feasible subdaily time series, and to analyse the rainfall concentration of all the individual rainfall events to finally obtain climate projection of extreme events (Section 3.4). This new method aims to help better understand the possible changes in the typical time-structure of subdaily rainfall events, not only for extreme events. In summary, the semi-stochastic approach consists of generating random subdaily data by using observed fractal features and physically consistent with the daily local climate projections. To obtain the IDF curves, extreme values are estimated from the daily time series in the direct method and from the subdaily time series in the semi-stochastic

FIGURE 3 General scheme of the methodologies used in this paper: links between the approaches (circles), main inputs (dark boxes), intermediate outputs–inputs (light boxes) and final output (box on the right). [Colour figure can be viewed at wileyonlinelibrary.com]
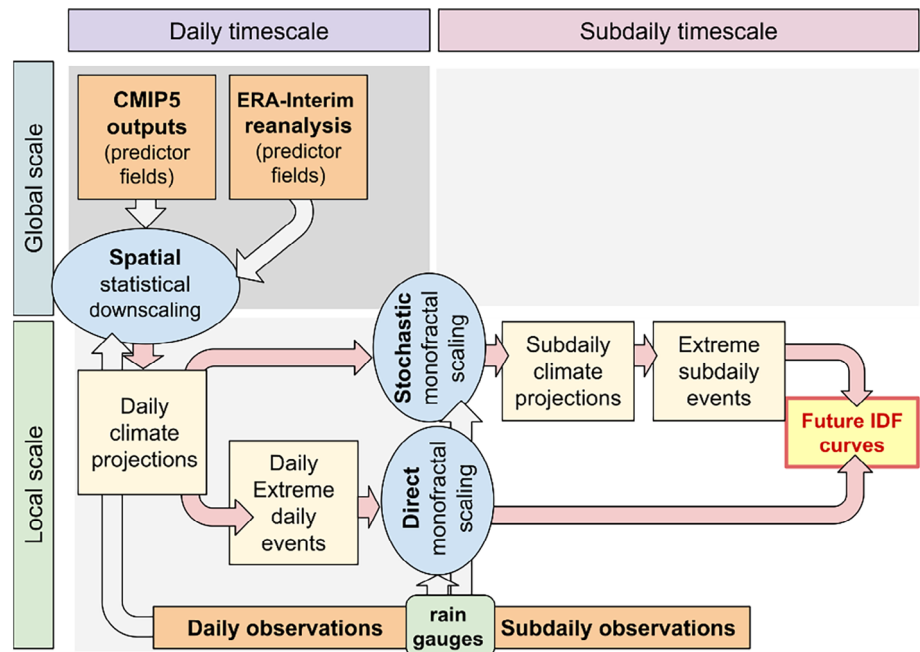
method (Figure 3). Details of all the methods used are described below.

3.2 | Spatial downscaling of daily values

We downscaled CMIP5 climate simulations using a statistical method that links *surface point observations* (from rain gauges) and *large-scale predictor fields* (obtained from the climate simulations). The spatial downscaling method uses a two-step analogue/transference approach, validated in international comparatives for climate models and reanalysis (Gutiérrez et al., 2019; Ribalaygua et al., 2013). The output of this spatial downscaling is directly the same point as the rain gauge of the time series used for training the method. However, the spatial distribution of the projected changes is obtained using the thin plate spline (TPS) interpolation approach. A summary of the statistical downscaling is presented here:

3.2.1 | Analogue stratification

The first step is based on an analogue stratification (Zorita and von Storch, 1999), applied to the CMIP5 climate simulations (Table 1); that is, the N most similar days to a target day (of the climate simulations) are selected from the ERA-Interim. The reanalysis is considered as a reference basis to reduce the nonlinearity in subsequent steps regarding the links between point observations and the atmospheric configurations that produce dry or wet days. In particular, the number was set as $N = 30$ according to

the previous studies (Monjo et al., 2016; Ribalaygua et al., 2013). The similarity between the 2 days (i.e., target and reference days) was measured using a weighted Euclidean distance (between CMIP5 model fields and ERA-Interim fields) in three nested synoptic windows by using six large-scale fields as predictors. The distance was calculated and standardized for each predictor by replacing it with the closest percentile of a reference population of distances for that predictor. The predictor fields used were wind speed and direction for both 1000 and 500 hPa, equally weighted, which represent the large-scale synoptic situation. To analyse the performance of the analogue stratification in the past, it was also applied to the ERA-Interim itself by cross-validation, disallowing the selection of similar days between the 7 days before and after each targeted day, and then obtaining analogue-based values compared to the target days. Temporal continuity of the downscaled ERA5-Interim enables to simulate past values in the entire time series even in dates when no observed values are recorded, thus avoiding gaps in the new reference data.

3.2.2 | Model output statistics

The second step applies three transfer functions to obtain increasingly refined precipitation amounts:

1. The earliest function is a set of N quotients of specific humidity at 700 hPa, estimated between each target day (simulated by the CMIP5 models) and their N analogous days (found from the ERA-Interim

reanalysis) over the vertical of a particular rain gauge (i.e., taking the closest grid points). This humidity field was chosen as a simplified indicator of the water content to predict precipitation amounts on rainy days. To consider better physical links, a group of $M = 30$ target days were downscaled together because it is assumed that climatic characteristics of rainfall vary little within a month of a particular year. For each of these targeted days, a 'preliminary precipitation amount' was obtained by averaging the precipitation amount (recorded in the observatory) of its N most analogous days, weighing by the target/analogous ratio of specific humidity at 700 hPa.

2. The second transfer function is a mixing process: The M target days are sorted from the highest to the lowest 'preliminary precipitation amount'. Then, all precipitation amounts of the weighted $M \times N$ analogous days are sorted and clustered in M groups to obtain a set of M 'refined precipitation amounts'. These quantities are assigned, in order, to the M days previously sorted by the 'preliminary precipitation amount' (Ribalaygua et al., 2013). The mixing process of the $M \times N$ analogous days ensures a better probability distribution of the final precipitation simulated within the set of M target days.

3. A final refinement procedure was applied to eliminate the residual systematic error of all climate simulations, by using parametric quantile mapping (Monjo et al., 2014, 2016). In this process, the ECDFs of the simulated time series were compared with the observed ECDFs. The theoretical cumulative distribution functions (F) were fitted to the ECDF of the daily time series (from observations and from the downscaled climate projections), applying inference with the profile log-likelihood approach (Monjo et al., 2014, 2016). To reduce the systematic errors of fit, several cumulative distribution functions were tested according to Monjo et al. (2016): two-, three- and four-parametric Gamma (Equation 7), Weibull (Equation 8), Gumbel (Equation 9), reversed Gumbel (Equation 10), log-logistic (Equation 11) and the three-parametric version of the GEV (Equation 12). After the bias correction of the downscaled climate outputs, the fitted theoretical functions were employed to obtain the daily values (x) for different return periods ($T = 1/[1 - F]$): 2, 5, 10, 25, 100 and 500 years.

$$F_1(x) = \frac{\gamma\left(h, \left(\frac{x-\xi}{\alpha}\right)^w\right)}{\Gamma(h)} \qquad (7)$$

$$F_2(x) = 1 - \exp\left(-\left(\frac{x-\xi}{\alpha}\right)^w - h\right) \qquad (8)$$

$$F_3(x) = \exp\left[-\exp\left(-\left(\frac{x-\xi}{\alpha}\right)^w - h\right)\right] \qquad (9)$$

$$F_4(x) = 1 - \exp\left[-\exp\left(\left(\frac{x-\xi}{\alpha}\right)^w + h\right)\right] \qquad (10)$$

$$F_5(x) = 1 - \frac{1}{1 + \left(\frac{x-\xi}{\alpha}\right)^{w + k\left(\frac{x-\xi}{\alpha}\right)}} \qquad (11)$$

$$F_6(x) = \begin{cases} \exp\left(-\left[1 - k\left(\frac{x-\xi}{\alpha}\right)\right]^{\frac{1}{k}}\right) & \text{if } k \neq 0 \\ \exp\left(-\exp\left(-\frac{x-\xi}{\alpha}\right)\right) & \text{if } k = 0 \end{cases} \qquad (12)$$

where $\alpha > 0$ is the scale, $w \geq 0$ and $k \geq 0$ are shape parameters, while ξ and h are the main and secondary positions (real numbers), respectively. The three-parametric versions of all of them are found for $h = 0$, while the two-parametric versions are additionally found for $w = 0 = h$, or setting k. Notice that, for $k = 0$, the GEV distribution becomes a two-parametric Gumbel distribution (type I). Reversed Weibull (type III) distribution is found if $\xi = -\alpha^{-1} < 0$. The KS test was used to discriminate which theoretical distribution performs better and to validate the downscaling of the climate model's outputs. KS p value < 0.05 was used for rejecting the null hypothesis that 'the samples are from the same population'. The uncertainty derived by the climate modelling was estimated for each emission scenario and also bounded by gathering the 20 projections (10 climate models $\times$ 2 emission scenarios) as a unique ensemble, due to the nonlinearity of mid-latitude precipitation patterns regarding the variation of temperature (i.e., some climate models show a higher increase in the extreme precipitation under the RCP4.5 than under the RCP8.5 because the higher temperature can lead to longer drier periods, with more evapotranspiration). Spatial distribution of that uncertainty was analysed by using a multi-projection ensemble of the interpolated downscaled outputs (TPS fields) and also in a separated way for each emission scenario.

3.3 | Direct time scaling

The scheme used is as follows: observed rainfalls are available and allow the calculation of the IDF curves with both subdaily and supradaily intensities. The
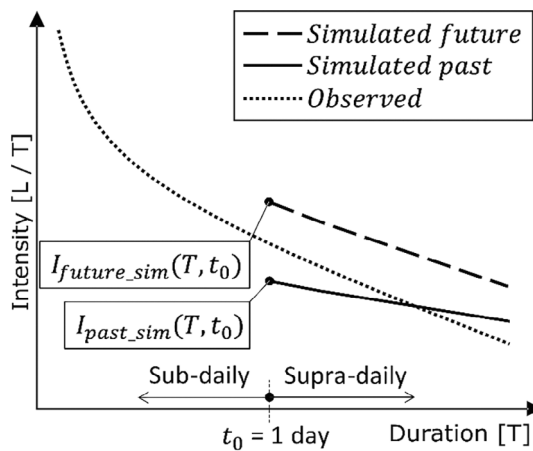
FIGURE 4 Conceptual scheme of how future and past (daily) projections derive changes in the supradaily IDF curves, while local observations establish the reference IDF curves for both subdaily and supradaily intensities. The climate change factor obtained on a supradaily timescale is then extrapolated to the subdaily scale by using the changes in the monofractal parameter ($\check{n}$). IDF, intensity–duration–frequency.

climate models provide past and future rainfall series with daily time steps, which allow the derivation of supradaily IDF curves (Figure 4), and it needs to be scaled to obtain the subdaily IDF curves.

Direct scaling was applied to the daily time series provided by the (spatially) downscaled model outputs (Section 4.1) to obtain CCF for rainfall intensities of durations down to 5 min. Therefore, future (I_f) and past (I_p) simulated rainfall intensities are the main variables. According to the *monofractal hypothesis*, the rainfall intensities scale is as follows (Monjo et al., 2014; Rodríguez-Solà et al., 2017):

$$I_i(T,t) = I_i(T,t_0)\left(\frac{t_0}{t}\right)^{\check{n}_i} \qquad (13)$$

where the subscript i refers to the future (f) or past (p) simulations, t_0 is the reference duration, that is $t_0 = 1$ day, while $\check{n}_i$ is the scaling factor in each case, obtained at subdaily (from 5 min to 1 day) and at supradaily (from 1 to 5 days) timescales. We do not use the same values for supradaily and subdaily scales, but the relative change (CCF) estimated from supradaily scales is assumed to be approximately the same at subdaily scales too, as an additional hypothesis of our work (Equation 14). Therefore, model-derived supradaily scaling factor $\check{n}_i$ was directly used to estimate changes in the subdaily parameter $\check{n}$. The rainfall intensities, $I_p(T, t)$ and $I_f(T, t)$, for different return periods, T, were obtained fitting several cumulative distributions according to Section 3.2 (Equations 7–12). Then, CCF is calculated

from these model-based IDF curves as a function of both return period T and duration t (Arnbjerg-Nielsen, 2012):

$$CCF(T,t) = \frac{I_f(T,t)}{I_p(T,t)} = \frac{I_f(T,t_0)}{I_p(T,t_0)}\left(\frac{t_0}{t}\right)^{\check{n}_f - \check{n}_p} \qquad (14)$$

To analyse the performance of the direct time scaling, the observed rainfall time series of Fabra was divided into two similar long periods: a first time period (1928–1975) and a second time period (1976–2021) were selected for cross-validation. Then, the CCFs were obtained in two different phases:

1. Using the original 5-min resolution rainfall time series and applying the following steps:
   ○ Extracting the first (1928–1975) and second (1976–2021) time series of the annual maximum value of different rainfall durations (from 5 min to 24 h).
   ○ Fitting the theoretical distributions to all the series to obtain the IDF curves.
   ○ Calculating the CCF as a ratio of the second versus the first set of sorted intensities.
2. Using the monofractal scaling applied to a daily rainfall time series and applying the following steps:

- Resampling the observed series into first (1928–1975) and second (1976–2021) daily series.
- Extracting a series of annual maximum of daily rainfalls from each one to obtain supradaily IDF curves.
- Applying monofractal downscaling to the supradaily IDF curves to obtain subdaily IDF curves.
- Calculating the CCF as a ratio of the second (1976–2021) versus the first (1928–1975) set of intensities of the downscaled IDF curves.

Finally, the CCF error introduced by the approach based on monofractal downscaling was calculated as the ratio between the CCF obtained with downscaling and the CCF obtained using the 5-min resolution rainfall time series (without downscaling). Logically, this validation process cannot be applied to the historical experiments of the climate models because subdaily values are not available from the climate model outputs. As a basis for the direct scaling, the empirical IDF curve (with observed value of $\check{n} \approx 0.74$) was used and then CCF quotient is applied to obtain projected IDF curves, whereby systematic errors tend to disappear.

3.4 | Semi-stochastic time scaling

Daily time series is obtained from the spatial downscaling (Section 3.1) and are used as a reference ('physical' time
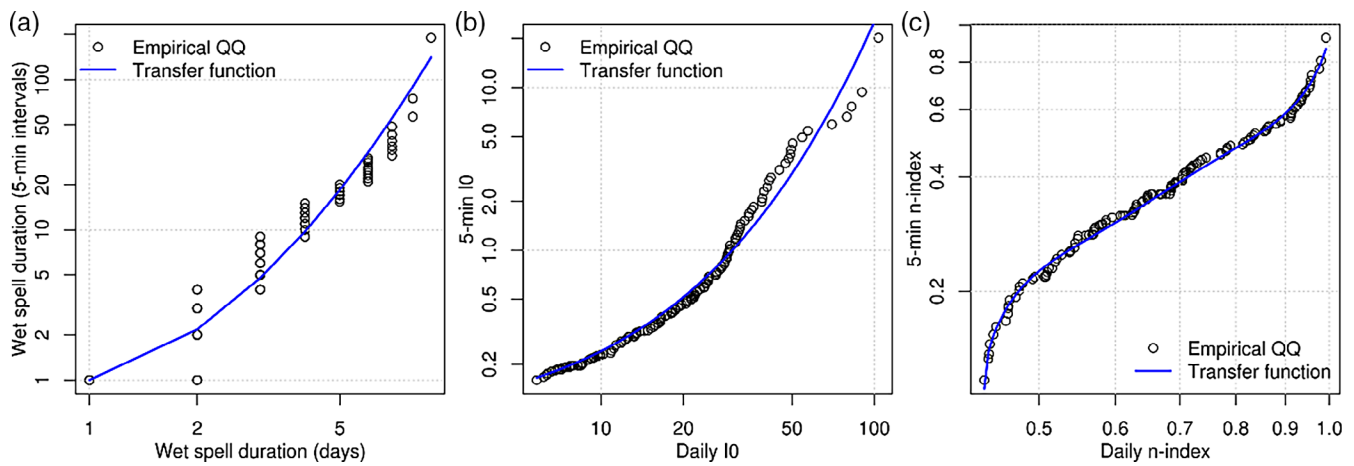
FIGURE 5 Example of empirical quantile–quantile mapping and theoretical transfer functions between daily and subdaily features: (a) wet spell duration, (b) average intensity (I_0) and (c) n-index values. [Colour figure can be viewed at wileyonlinelibrary.com]

series) for combining with a purely stochastic time series. Subdaily time series were simulated using statistical features of the concentration n-index. A total of four steps were designed here to obtain the subdaily time series from the daily time series:

1. The first step comprised aggregating the observed 5-min values of rainfall into a simple daily time series (summing all the rainfall records of each day) to fit transfer functions to the empirical quantile–quantile mapping (between both timescales) for three main features (according to Equation 6): (i) wet spell duration, (ii) fitting reference intensity I_0 and (iii) fitting n-index (Figure 5). At this stage, only original rain-gauge values (i.e., without gap filling) could be used to find empirical relationships between the subdaily and daily scales.

2. All the transfer functions are applied to every (observed or simulated) daily time series to obtain the hypothetical features for the subdaily timescale, maintaining statistically significant relations among them. That is, the distribution of the n-index can depend on the distribution of rainfall intensities or wet spell durations, so the distributions were simulated regarding these time structure relationships using stepwise regression plus a random generator. From the second step onward, it can also applied to all the 'physical' time series.

3. Entire time series of feature values are randomly simulated from the distribution functions obtained in Step 2. This step has three substeps: (i) First, a time series of 'wet/dry spell' is obtained; (ii) then the time series of 'n-index' and 'reference intensity' values are generated, both with the same length as that of the wet spell and (iii) finally, the 5-min values of rainfall are obtained for each wet spell (synthetic hyetograph)

according to the previous 'n-index' and 'reference intensity' sequences.

4. The stochastic time series generated in Step 3 is aggregated at a daily scale to compare with the (complete) daily time series obtained from the downscaled model outputs ('physical' time series). Both these daily time series are sorted to identify the rescaling factors applied to the subdaily values of the stochastic series for each day, according to the physical series. The corrected sequence of subdaily values becomes the final semi-stochastic time series, with the same daily amounts as the physical series (Figure 6).

Similar to the simulation validation applied to daily values, the KS test was also computed to check the goodness of the semi-stochastic scaling of subdaily values. This includes simulating the other rainfall features (n-index, reference intensities and wet/dry spell duration). Finally, IDF curves are estimated from the simulated time series and thus CCF according to Equation (14) by estimating the probable maximum intensity and the fractal parameter $ň$, which are respectively equivalent to reference intensity (I_0) and the n-index of a synthetic rainfall event given by each return period.
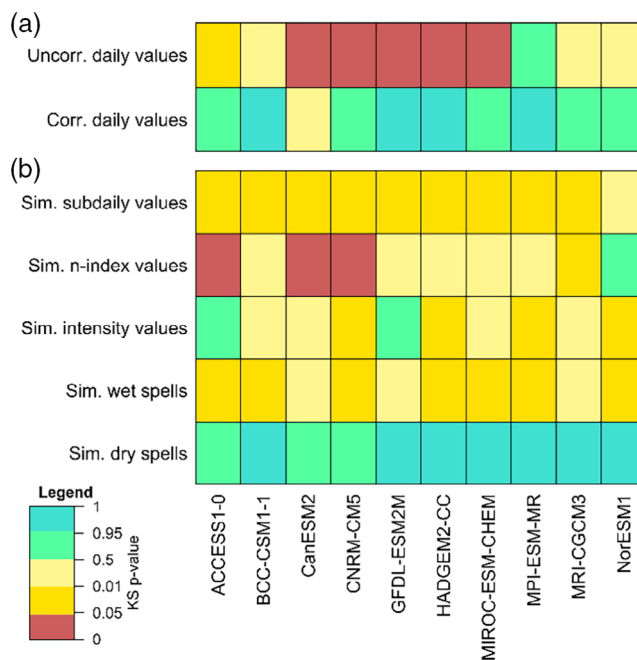
4 | RESULTS

4.1 | Validation of methods

4.1.1 | Spatial downscaling of daily values

According to the KS test, the spatial downscaling obtained good performance for simulating the probability
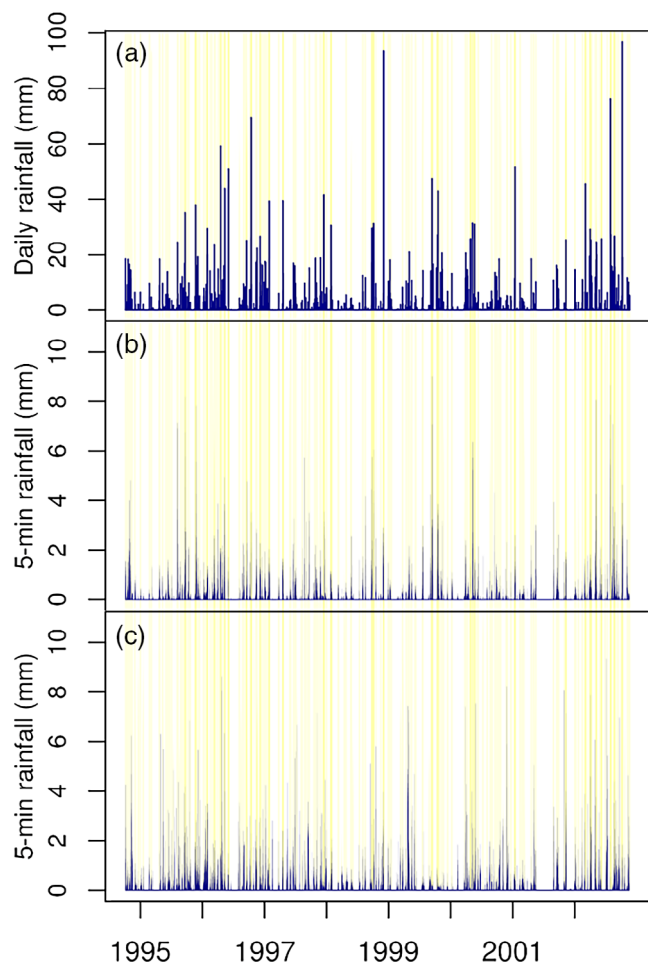
FIGURE 6 Example of semi-stochastic generation of subdaily rainfall for Barcelona: (a) daily time-series observed, (b) subdaily time-series observed and (c) subdaily time-series simulated. Dark bars are all the rainfall values, while light shaded areas (represent rainy days > 0.1). Notice that the lower panel does not intend to reproduce the observed values one by one, since it is stochastic at a subdaily scale and deterministic at a daily scale (given by the physical simulation of the daily values before disaggregating). [Colour figure can be viewed at wileyonlinelibrary.com]

FIGURE 7 Kolmogorov–Smirnov (KS) *p* value of the validation process for 10 downscaled CMIP6 outputs compared to observed probability distribution. The model outputs are: (a) uncorrected and corrected daily rainfall values and (b) semi-stochastic simulation of 5-min rainfall features (rainfall values, *n*-index values, reference intensities, wet spells and dry spells). KS *p* value < 0.05 is used for rejecting (red boxes) the null hypothesis (the samples are from the same population). CMIP6, Coupled Model Intercomparison Project Phase 6. [Colour figure can be viewed at wileyonlinelibrary.com]

4.1.2 | Direct time scaling

As regards the direct scaling applied to the daily time series (observed or provided by the spatially downscaled model outputs), the CCF presented an expected systematic error as a function of rainfall duration, obtained from the cross-validation (Section 3.3, step 1). Comparing the results obtained with temporal downscaling and with the original subdaily data, the systematic error is negative, which is interpreted such that the CCF obtained by direct downscaling is underestimated compared to the obtained from actual subdaily values (Figure 8a). The errors have lower values (<5%) ranging between 0- and 120-min durations, then they increase up to a peak value at approximately 360 min (about 10%–20%), and reduce with increasing duration (down to 5%–10%), ranging errors with the return period (Figure 8b).

This underestimation obtained by downscaling the (calendar) daily time series is partially due to the difference between the aggregated rainfall values (in daily time series) and the actual rainfall values for a duration of 24 h. In fact, the 24-h rainfall is generally greater than

distribution of daily precipitation in Barcelona, comparing downscaled historical outputs of five climate models (ACCESS1-0, BCC-CSM1-1, MPI-ESM-MR, MRI-CGCM3, and NorESM1-M) to the observed probability distribution (Figure 7a). The other model outputs (CanESM2, CNRM-CM5, GFDL-ESM2M, HADGEM2-CC, and MIROC-ESM-CHEM) did not pass the KS test for the positive values of precipitation in some seasons. However, after the correction (Section 3.2.1, step 3), all of them passed the KS test for the entire time series. Moreover, the maximum daily precipitation is also well simulated by most of the model outputs compared to the observed reference values, with a systematic error smaller than 10% in all cases.
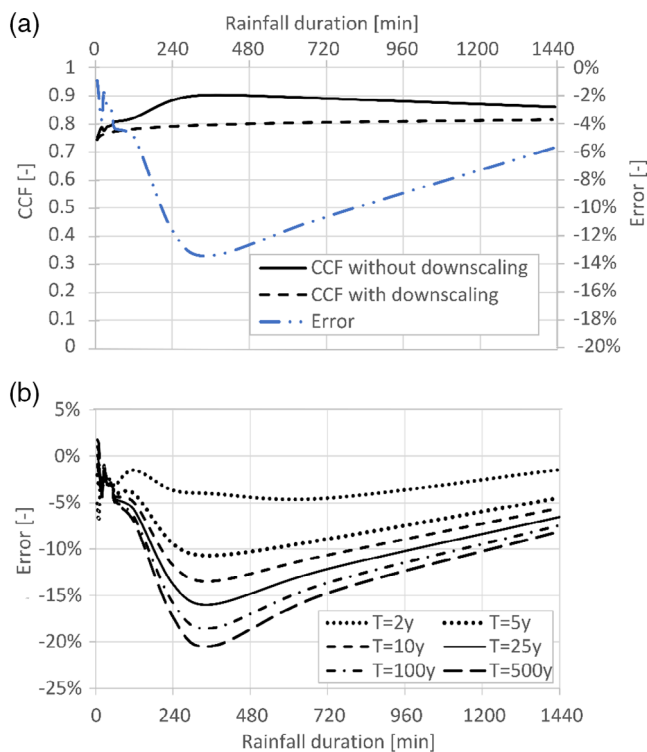
FIGURE 8 Validation process for the direct-scaling approach applied to the observed time series: (a) example of CCF obtained for a 10-year return period with temporal downscaling applied to calendar daily data compared to the CCF of the original subdaily data (marked as 'without temporal downscaling'), and the error introduced when the downscaling approach is used, and b) the difference (error) between the CCF calculated on downscaled and not-downscaled values. This example corresponds to the CCF of the 1976–2021 period compared to the 1928–1975 period. CCF, climate change factor. [Colour figure can be viewed at wileyonlinelibrary.com]

the 1-day values because the usual duration of extreme precipitation within a calendar day is about 4–12 h on average (Llasat, 2001; Morbidelli et al., 2020). According to Equation (14), using a climatic average (e.g., $\check{n} = 0.5$), the 24 h/1 day differences can be up to 100%. However, the differences are less than 20% in all cases because the systematic errors of rainfall measure (1 day vs. 24 h) and of $\check{n}$ parameter almost disappear when the CCF quotient is used, especially for durations shorter than 2 h. Therefore, we used this duration as the primary time scale for the CCF analysis.

4.1.3 | Semi-stochastic time scaling

Subdaily rainfall is well simulated for Barcelona at a time resolution of 5 min. That is, the probability distribution of wet spell precipitation and n-index values (see, for instance, Figure 4) passed the KS test for most cases,

comparing historical experiments of the multi-model approach and the observed time series (Figure 7b). However, three downscaled climate models (ACCESS1-0, CanESM2 and CNRM-CM5) presented difficulties in simulating the n-index for wet spells. Despite this problem, the bias of the n-index distribution is zero and, therefore, it does not affect the results (because the method of applying empirical transfer functions is unbiased).

4.2 | Projection of the climate change factors

An increment in 12-h extreme rainfall up to 30%–40% is projected for 2071–2100, according to both time scaling techniques applied to the (spatially downscaled) climate model outputs. Specifically, the return period of annual maximum 12-h extreme values was analysed for the study area (Figure 9). Statistical significance of this increment is found especially in the inner of the region for 2-year and 10-year return periods for the 2041–2070 period and for the 2-year to 100-year return periods by the end of the century.

Analysing the climate change in a separated way for each emission scenario, projections of the IDF curves showed significant changes according to the semi-stochastic monofractal scaling for both scenarios (Figure 10). In 75% of the cases, the CCF is higher than 1, ranging up to 1.4 or 1.5 for the higher return periods, especially in the 2071–2100 period under the RCP8.5 scenario. The uncertainty levels are lesser for the RCP8.5 than for the RCP4.5 scenario in the 2041–2070 and 2071–2100 periods. However, results for monofractal time scaling show that the median climate of CCFs for all the cases is practically equal to one in the period 2011–2040 and then increases to values above one in the 2041–2070 and 2071–2100 periods (Figure 11). In addition, the median of CCFs presents similar values for all the extreme events except for the 2011–2040 period under the RCP4.5 scenario and the 2071–2100 period under the RCP8.5 scenario, where the higher the return period, the higher the median of the CCFs. The uncertainty bounds of CCFs also increase from the 2011–2040 to 2041–2070 periods and finally to the 2071–2100 period.

Overall, the results showed two differentiated main results: on the one hand, a high uncertainty comparing both methods for the early 21st century (2011–2040 average) with no significant changes according to the direct-scaling approach and some climate change signal for the higher return periods if the semi-stochastic approach is considered. On the other hand, the subdaily patterns are clearer for the medium period (2041–2070) with a consensual increase in the CCF according to both methods. The CCF ranges between 1 and 1.3 for all the return

FIGURE 9 Multi-projection ensemble of extreme precipitation: median of changes in extreme events of 12-h precipitation projected for the Ter-Llobregat system, according to 2-year, 10-year, and 100-year return periods (rows) and for three future time periods (2011–2040, 2041–2070 and 2071–2100, second to fourth columns) with respect to the reference period 1976–2005 (first column) by using the semi-stochastic approach. Significant changes (p values < 0.05) are highlighted with dotted shadow areas. [Colour figure can be viewed at wileyonlinelibrary.com]
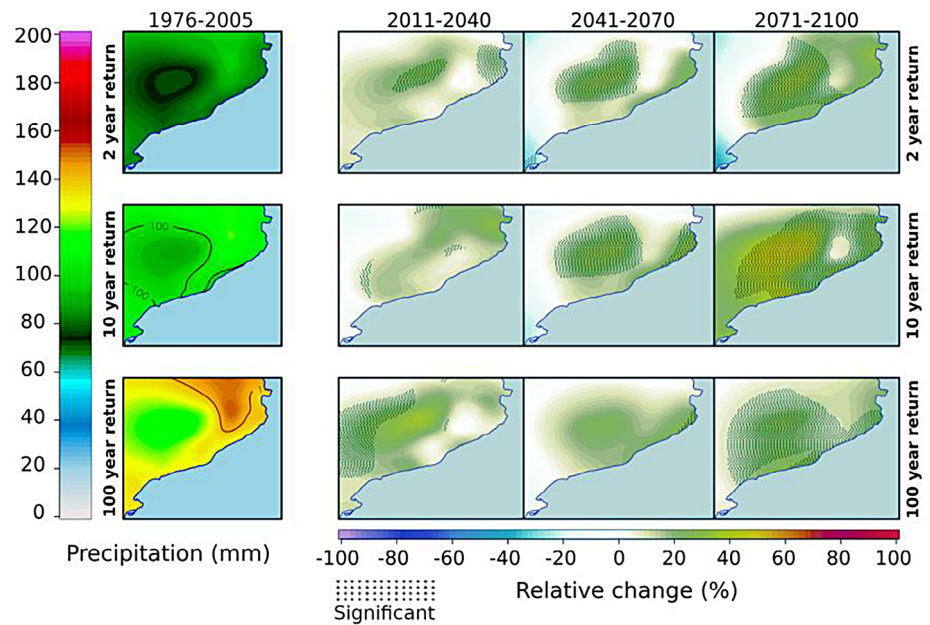
periods within the projected 2-h extreme event. At the end of the century (2071–2100), the uncertainty is high again, but some consensus is obtained for the higher return periods with a CCF up to 1.5 for 1-h extreme events. Similar results were found for the Barcelona metropolitan area and the inner region of Barcelona (not shown).

5 | DISCUSSION

5.1 | Strengths and weaknesses

From the assumption of fractal self-similarity between daily and subdaily timescales, it is expected that stochastic downscaling of subdaily precipitation inherits the geometrical (and therefore some physical) features of the time structure of the daily rainfall; that is, it was possible to find statistical relationships between 'how rainfall is concentrated within a multiday event' and 'how rainfall is concentrated within a day' (as a result of the observed time series). For this purpose, two monofractal approaches were analysed, with some pros and cons. The advantages of the direct method are the simplicity of calculation (with less computational cost); however, it does not allow the evaluation of the performance of each climate model to simulate the temporal concentration of the precipitation because it is applied directly to the model outputs. It can only be validated using the observed subdaily time series by simulating a CCF between two separated historical parts. In contrast, the semi-stochastic approach simulates subdaily time series for each climate model, which allows a comparison of the historical simulation of the climate models with the

observed subdaily time series regarding the rainfall features (n-index, wet/dry spells and reference intensities). Nevertheless, the physical part of the semi-stochastic technique is limited to the day-to-day combination of the stochastic subdaily time series with the daily time series simulated with the spatial downscaling (which uses atmospheric fields as physical predictors).

As a positive point of that combination, the good performance of the spatial downscaling of precipitation ensures low systematic errors (less than 10%) in the daily time scale for Barcelona and passing the KS test in more than 75% of the cases (combination between historical experiments and daily rainfall features). Similar confidence is obtained for the semi-stochastic monofractal approach with an adequate simulation of the subdaily rainfall features (wet/dry spells, maximum intensities and n-index). The validation of the direct scaling of the CCF also provides an idea of the errors that are introduced when the method is applied to daily series with a general underestimation for all the durations (between 0% and 20%) and with low values (<5%) for periods shorter than 2 h.

Of course, the large set of required calculus makes semi-stochastic technique has much high computational cost than the direct approaches. A key idea of this work is to check whether consensual changes are projected under both simple and sophisticated methods, and another important point is to analyse their systematic contribution to the uncertainty cascade (i.e., in the validation process and in the statistical significance of the projected climate signal). The added value of the semi-stochastic technique is that enables to estimate not only extreme events but also statistics of general subdaily wet spells, for example, to estimate rainfall concentration and
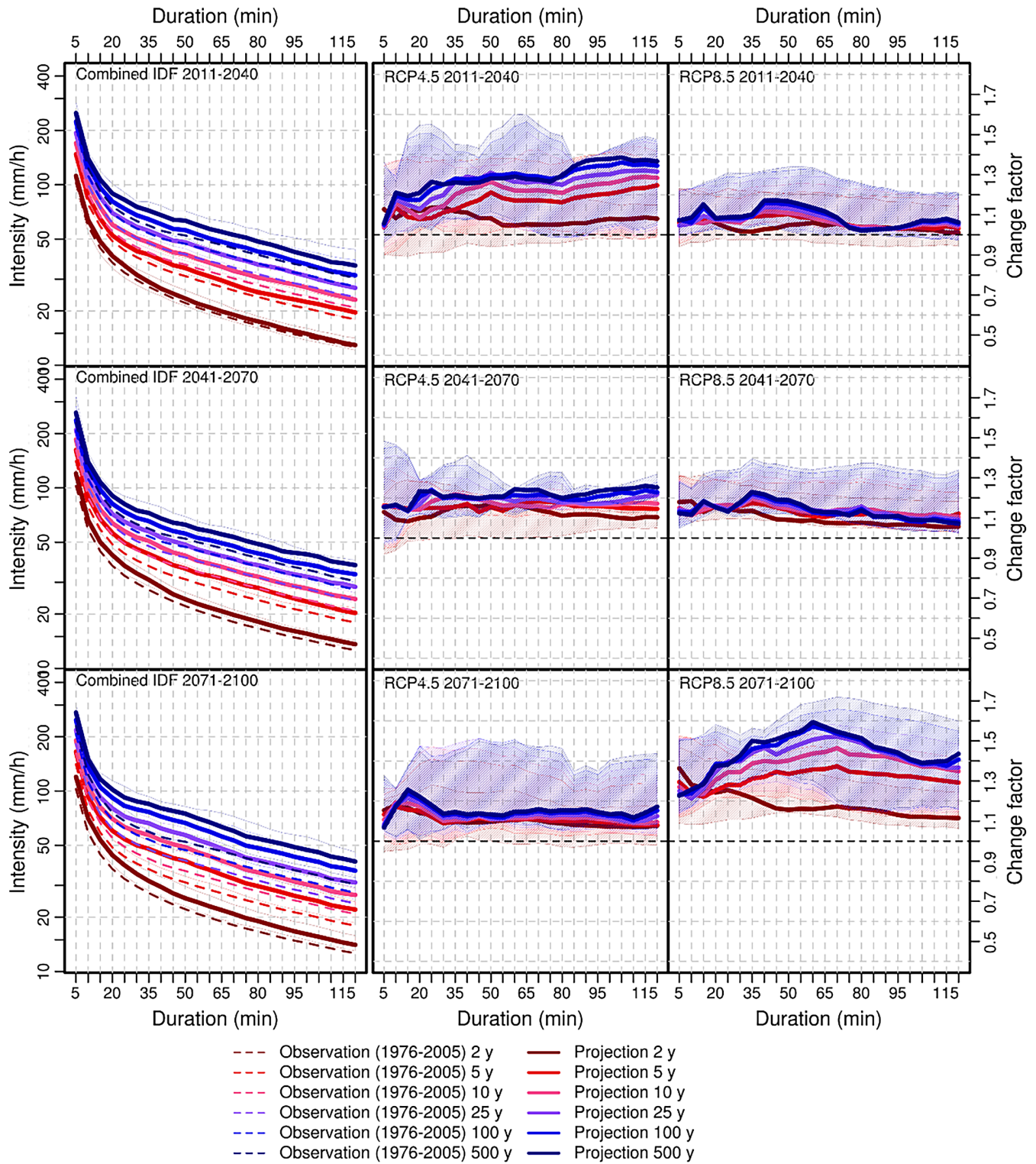
FIGURE 10 Projected IDF curves for Barcelona city according to absolute values (first column) and the change factor (second and third columns) for three future periods: 2011–2040 (top), 2041–2070 (centre) and 2071–2100 (bottom), according to the semi-stochastic monofractal time scaling. The figure shows a multi-projection ensemble of IDF curves by combining the downscaled outputs of 10 climate models and two emission scenarios (RCP4.5 and RCP8.5), where lines representing the median and shaded areas indicating the 25th and 75th percentiles as a function of different rainfall durations. Dashed lines correspond to the empirical IDF curves (from the observed 1976–2005 period), used as a reference to correct the simulated IDF curves under the CMIP5 *Historical* experiment (also for the 1976–2005 period). CMIP5, Coupled Model Intercomparison Project Phase 5; IDF, intensity–duration–frequency. [Colour figure can be viewed at wileyonlinelibrary.com]
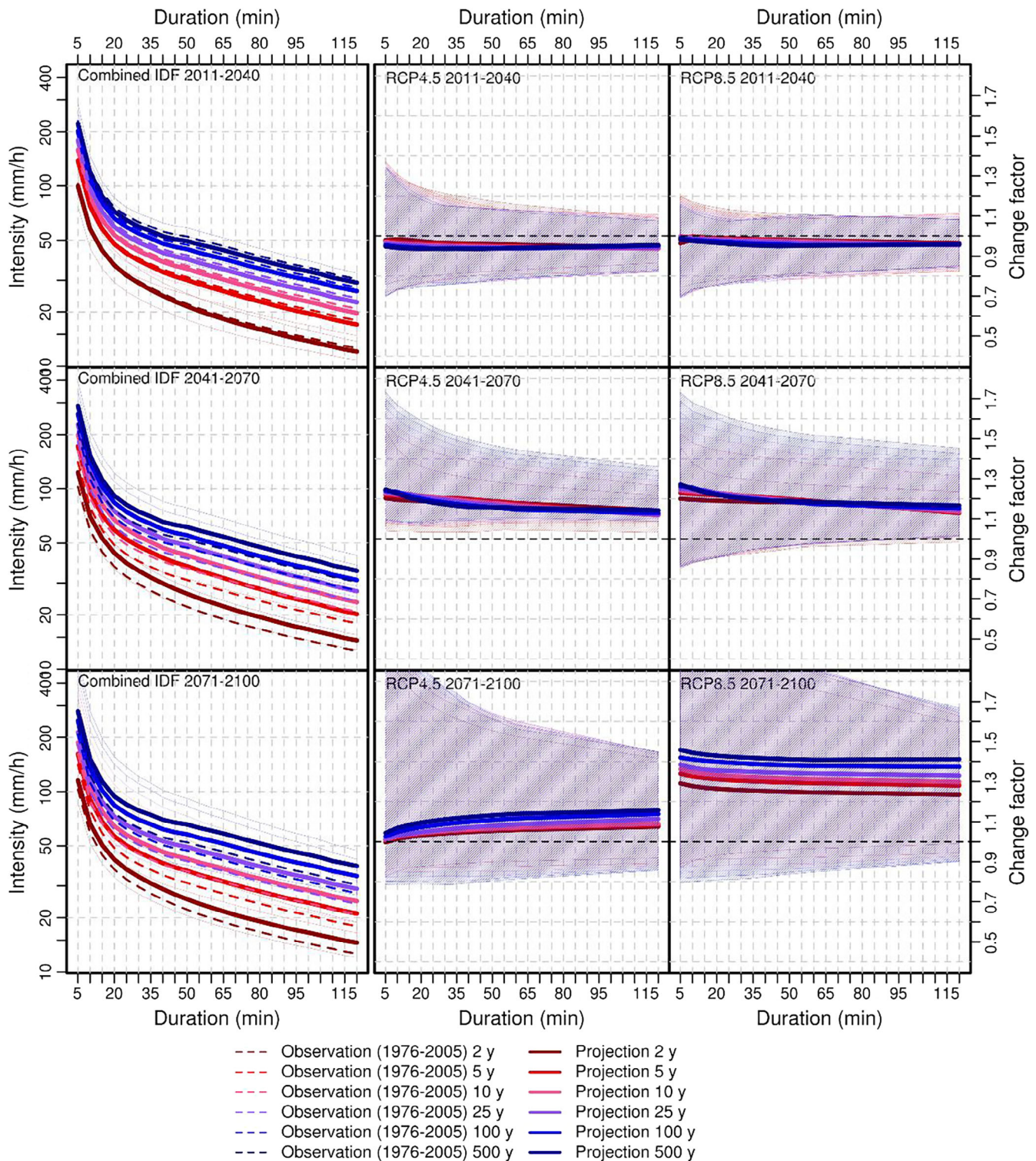
FIGURE 11 Same as Figure 10 but using the direct monofractal approach. [Colour figure can be viewed at wileyonlinelibrary.com]

its hydrological effects. Notice that some hydrological models need entire (subdaily) time series instead of just synthetic hyetographs from IDF curves (Ficchì et al., 2019), and therefore semi-stochastic techniques could be applied to project future hydrological features at subdaily scales.

5.2 | Significant changes

After correcting the systematic errors of the final IDF curves, random errors remained in the uncertainty cascade. They were evaluated using the multi-model approach with two emission scenarios, which showed a
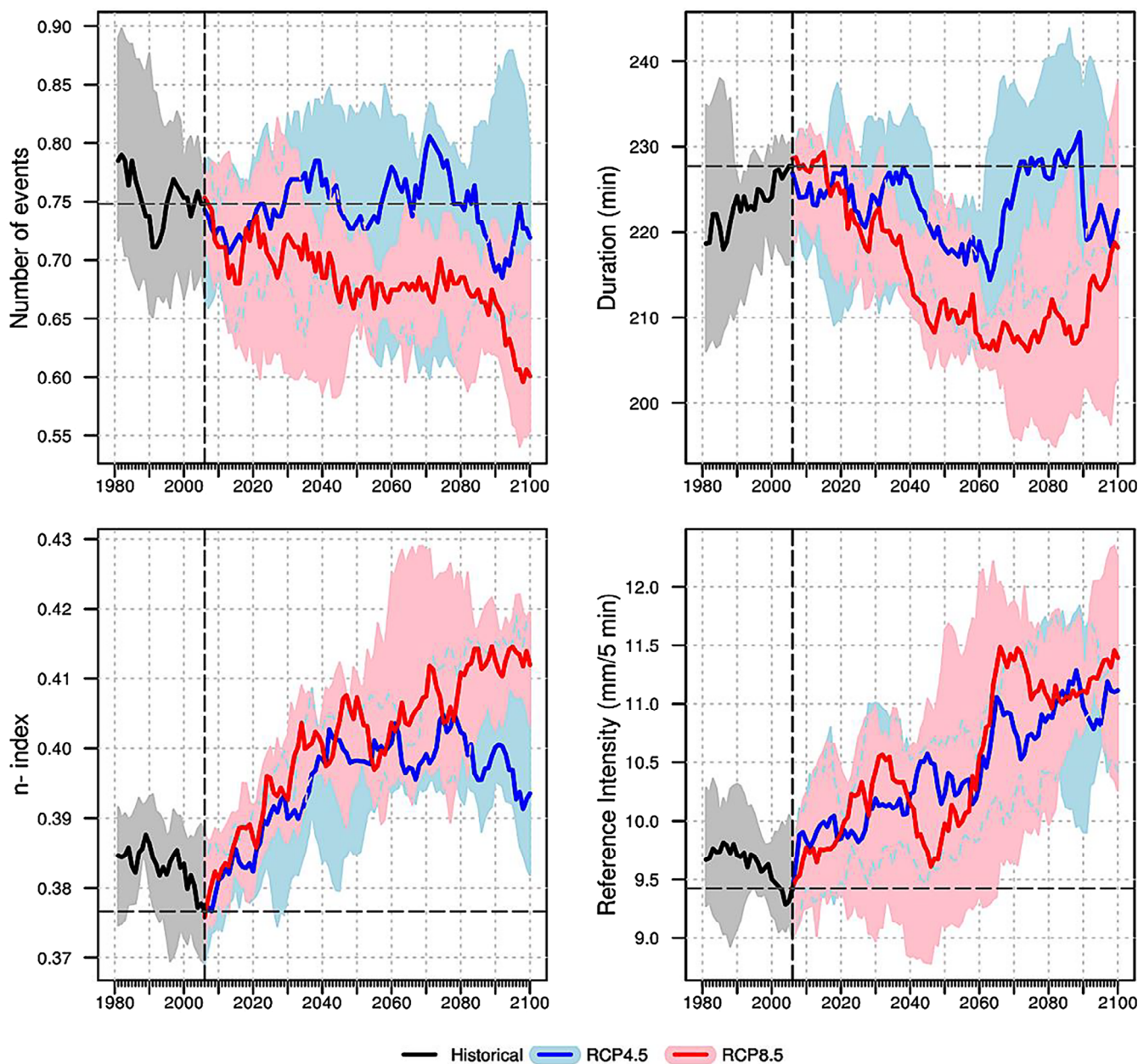
FIGURE 12 Multi-ensemble projection of subdaily wet spells with precipitation amounts higher than 50 mm in Barcelona (set of 27 stations): Number of events (top-left), duration (top-right), *n*-index (bottom-left) and reference intensity (bottom-right). The ensemble median (solid lines) and the 10th–90th percentile values (shaded areas) are displayed. The vertical dashed line marks the end of historical data (2005). [Colour figure can be viewed at wileyonlinelibrary.com]

0%–30% variation range for the CCF. Therefore, the systematic error of the methods (about 5%–10%) is lower than the expected increase in subdaily intensities for IDF curves in Barcelona. According to the two analysed methods, a CCF of about 1.15 ± 0.15 is expected for the 2041–2070 period in all the return periods between 2 and 500 years. This result is similar to the previous analysis obtained for Barcelona at a subdaily scale using CMIP4 climate models, which projected a CCF between 1 and 1.1 for low-emission scenarios and between 1.1 and 1.3

under the worst scenarios (Rodríguez et al., 2014). Moreover, these changes are consistent with the projection of 12-h extreme precipitation in the 27 rain gauges located in the watershed of Ter-Llobregat system around Barcelona, which will experience an increase of up to 10%–20% in the 2041–2070 period and 20%–40% in the 2071–2100 period (Monjo et al., 2019). An exception is found for 10-year return-period 12-h rainfall by the 2071–2100 period, for which an increase higher than 40% is projected (Figure 9), in contrast with the projection of less

than 30% in 2-year and 100-year return-period values (consistent with the projection of CCF up to 2-h duration under both methods). This conclusion is also consistent with the increase in the n-index projected for the wet spells in Barcelona, showing a change up to 8%–10%, from $n = 0.38$ to $n = 0.41$, especially under the RCP8.5 scenario (Figure 12 shows the wet spells of more than 50 mm, but projections are also similar for more than 2 mm).

Results showed consensual changes in extreme events and moreover, the simulation of the monofractal parameter ($ň$) by the direct scaling is consistent with the obtained from the statistics of individual rainfall events (n). This result validates the initial assumption used in the direct scaling, that is, the change of the parameter $ň$ at subdaily scales can be approximated by the changes of the parameter $ň$ obtained from supradaily scales (Equation 14). In general terms, the physical coherence and the consensus between the results of both methods show that the analysis of CCF is robust under the monofractal hypothesis, despite the complexity of the Barcelona rainfall regimes.

On a daily scale, Monjo et al. (2016) found a slight possible increase in extreme precipitation for return periods between 10 and 100 years under the RCP4.5 scenario, but with low statistical significance (Monjo et al., 2016). In fact, the RCP8.5 scenario projects a decrease in the daily precipitation (consistent with the lower amount of annual rainfall) with shorter wet spell durations and longer drought periods due to more evapotranspiration (Gaitán et al., 2020). In summary, some climate models showed a higher increase in extreme precipitation under RCP4.5 than under RCP8.5, and therefore both ensembles project a similar increase in rainfall concentration (as shown in Figure 12). The physical interpretation is that mid-latitude precipitation patterns are nonlinear with the variation of temperature. A warmer atmosphere increases both the evapotranspiration potential and the atmospheric water content, and therefore the variation of precipitation depends on their local balance. More specifically, the return period of a particular precipitation amount is given by the balance between the increase of the rainfall intensity within an event (determined by specific humidity) and the reduction of the number of wet events (determined by some synoptic-scale atmospheric situations). Figure 12 shows that both emission scenarios converge in a similar way for the maximum reference intensity projected for the end of century (about +20%) but with a little more concentration (i.e., higher n-index) under the RCP8.5 scenario.

On the other hand, a higher fractal dimension of rainfall in the Mediterranean region is associated with more frequent anticyclonic regimes (Meseguer-Ruiz et al., 2019). Therefore, the increment of the n-index is consistent with the poleward expansion of the Hadley cell that affects the Southern Europe (Hu & Fu, 2007; Yang et al., 2020).

6 | CONCLUSIONS

To obtain the CCF of 5-min-resolution IDF curves from local climate scenarios on a daily scale, this paper compares two monofractality-based methods: a semi-stochastic method and a direct method. For both, the validation process showed that systematic errors (5–10%) are smaller than the climate change signal (about 15%–30%). This result allows the measurement of changes in rainfall concentration (linked to the monofractal dimension) and in intensity distribution (as a basis of IDF curves). As an example of the application of the methods, an increase in rainfall concentration/intensity is obtained by analysing local climate scenarios for reference time series with a Mediterranean climate (with high climate variability).

Completing the discussion for the studied area, the general conclusion is that the hydrological cycle is accelerating with more evapotranspiration impacting on the longest rainfall regimes (reduction of rainfall amounts from the day to the century timescales) and more available atmospheric water content during the wet subevents (within the more extreme rainfall episodes, shorter than 2 h). Moreover, the increase of rainfall fractality, concentration or inequality (in temporal and spatial distribution) is linked to more frequent anticyclonic weather regimes in the Mediterranean regions.

Despite the advances in earth system modelling (from CMIP4 to CMIP5 experiments), the new results obtained through the two techniques project trends similar to those found in previous studies for Barcelona. This consistency of the results is especially relevant for policy makers as it provides robustness in decision-making regarding the design of stormwater management infrastructure. In this case, the consensual result of both monofractal approaches showed that the rainfall regime of Barcelona would be 8%–10% more concentrated in short periods, and therefore more intense with increases in maximum rates for 2-h periods of up to 15% or 30%. However, some systematic uncertainties are found when both methods are compared. For instance, the semi-stochastic technique projects an increase higher than 40% for 10-year return-period 12-h rainfall by the 2071–2100 period, which could be an overestimation compared to 2-year and 100-year return period, because they project an increase lower than 30%, like the direct scaling for 2-h durations.

After this analysis, further research will focus on the possible generalization of both the semi-stochastic and direct approaches to incorporate multifractal analysis. In this case, it is expected that the modification of the methods could introduce a second-order correction because the theoretical functions used showed an adequate goodness-of-fit (passing KS tests) for simulating extreme rainfall between 5 and 120 min. Therefore, although the methods are applied to a few reference time series in Spain, it is expected that they will be applicable to any time series.

AUTHOR CONTRIBUTIONS

Robert Monjo: Conceptualization; methodology; validation; investigation; writing – original draft; writing – review and editing; formal analysis; visualization. **Luca Locatelli:** Methodology; investigation; validation; visualization; writing – review and editing; writing – original draft; formal analysis. **John Milligan:** Methodology; validation; investigation; formal analysis. **Luis Torres:** Writing – review and editing; investigation; formal analysis. **Marc Velasco:** Conceptualization; funding acquisition; formal analysis; supervision; resources; methodology; project administration; investigation. **Emma Gaitán:** Investigation; methodology; validation; formal analysis. **Javier Pórtoles:** Data curation; formal analysis; validation; investigation; software. **Darío Redolat:** Writing – review and editing; investigation; validation. **Beniamino Russo:** Methodology; resources; conceptualization; formal analysis; investigation. **Jaime Ribalaygua:** Resources; funding acquisition; investigation; validation; formal analysis; project administration.

DATA AVAILABILITY STATEMENT

Final downscaled projections are available at daily and subdaily time scales in Monjo et al. (2020).

ORCID

Robert Monjo https://orcid.org/0000-0003-3100-2394
Darío Redolat https://orcid.org/0000-0001-9621-8730

REFERENCES

Arnbjerg-Nielsen, K. (2012) Quantification of climate change effects on extreme precipitation used for high resolution hydrologic design. *Urban Water Journal*, 9, 57–65. Available from: https://doi.org/10.1080/1573062X.2011.630091

Bäcker, A., Haque, M. & Khaymovich, I.M. (2019) Multifractal dimensions for random matrices, chaotic quantum maps, and many-body systems. *Physical Review E*, 100, 032117. Available from: https://doi.org/10.1103/PhysRevE.100.032117

Bara, M., Gaál, L., Kohnová, S., Szolgay, J. & Hlavčová, K. (2010) On the use of the simple scaling of heavy rainfall in a regional estimation of IDF curves in Slovakia. *Journal of Hydrology and Hydromechanics*, 58, 49–63. Available from: https://doi.org/10.2478/v10098-010-0006-0

Barbero, R., Fowler, H.J., Lenderink, G. & Blenkinsop, S. (2017) Is the intensification of precipitation extremes with global warming better detected at hourly than daily resolutions? *Geophysical Research Letters*, 44, 974–983. Available from: https://doi.org/10.1002/2016GL071917

Bi, D., Marsland, S., Uotila, P., O'Farrell, S., Fiedler, R., Sullivan, A. et al. (2013) ACCESS OM, the ocean-sea ice core of the ACCESS coupled model. *Australian Meteorological and Oceanographic Journal*, 63, 213–232. Available from: https://doi.org/10.22499/2.6301.008

Bonsoms, J., Gonzalez, S., Prohom, M., Esteban, P., Salvador-Franch, F., López-Moreno, J.I. et al. (2021) Spatio-temporal patterns of snow in the Catalan Pyrenees (NE Iberia). *International Journal of Climatology*, 41, 5676–5697. Available from: https://doi.org/10.1002/joc.7147

Burgueño, A., Codina, B., Redaño, A. & Lorente, J. (1994) Basic statistical characteristics of hourly rainfall amounts in Barcelona (Spain). *Theoretical and Applied Climatology*, 49, 175–181. Available from: https://doi.org/10.1007/BF00865532

Casas, M.C., Rodríguez, R.M., Prohom, M., Gázquez, A. & Redaño, A. (2011) Estimation of the probable maximum precipitation in Barcelona (Spain). *International Journal of Climatology*, 31, 1322–1327. Available from: https://doi.org/10.1002/joc.2149

Casas-Castillo, M.C., Llabrés-Brustenga, A., Rius, A., Rodríguez-Solà, R. & Navarro, X. (2018) A single scaling parameter as a first approximation to describe the rainfall pattern of a place: application on Catalonia. *Acta Geophysica*, 66, 415–424. Available from: https://doi.org/10.1007/s11600-018-0122-5

Casas-Castillo, M.C., Rodríguez-Solà, R., Navarro, X., Russo, B., Lastra, A., González, P. et al. (2018) On the consideration of scaling properties of extreme rainfall in Madrid (Spain) for developing a generalized intensity-duration-frequency equation and assessing probable maximum precipitation estimates. *Theoretical and Applied Climatology*, 131, 573–580. Available from: https://doi.org/10.1007/s00704-016-1998-0

Chan, S., Kendon, E., Fowler, H., Blenkinsop, S. & Roberts, N. (2014) Projected increases in summer and winter UK sub-daily precipitation extremes from high-resolution regional climate models. *Environmental Research Letters*, 9, 084019.

Chow, V.T. (1962) *Hydrologic determination of waterway areas for drainage structures in small drainage basins*. Urbana, IL:

Engineering Experiment Station, University of Illinois. (Bulletin No. 462).

Chylek, P., Li, J., Dubey, M.K., Wang, M. & Lesins, G. (2011) Observed and model simulated 20th century Arctic temperature variability: Canadian Earth System Model CanESM2. *Atmospheric Chemistry and Physics Discussions*, 11, 22893–22907. Available from: https://doi.org/10.5194/acpd-11-22893-2011

Collins, W.J., Bellouin, N., Doutriaux-Boucher, M., Gedney, N., Hinton, T., Jones, C. D., et al. (2008) *Evaluation of the HadGEM2 model*. Hadley Centre Technical Note HCTN 74. Met Office Hadley Centre, Exeter, UK.

Cordery, I. & Pilgrim, D.M. (1984) Time patterns of rainfall for estimating design floods on a frequency basis. *Water Science and Technology*, 16, 155–165.

D'Onofrio, D., Palazzi, E., von Hardenberg, J., Provenzale, A. & Calmanti, S. (2014) Stochastic rainfall downscaling of climate models. *Journal of Hydrometeorology*, 15, 830–843. Available from: https://doi.org/10.1175/Jhm-D-13-096.1

Dunne, J.P., John, J.G., Adcroft, A.J., Griffies, S.M., Hallberg, R.W., Shevliakova, E. et al. (2012) GFDL's ESM2 global coupled climate–carbon earth system models. Part I: physical formulation and baseline simulation characteristics. *Journal of Climate*, 25, 6646–6665. Available from: https://doi.org/10.1175/JCLI-D-11-00560.1

Ficchì, A., Perrin, C. & Andréassian, V. (2019) Hydrological modelling at multiple sub-daily time steps: model improvement via flux-matching. *Journal of Hydrology*, 575, 1308–1327. Available from: https://doi.org/10.1016/j.jhydrol.2019.05.084

Gaitán, E., Monjo, R., Pórtoles, J. & Pino-Otín, M.R. (2020) Impact of climate change on drought in Aragon (NE Spain). *Science of the Total Environment*, 740, 140094. Available from: https://doi.org/10.1016/j.scitotenv.2020.140094

Galmarini, S., Steyn, D.G. & Ainslie, B. (2004) The scaling law relating world point-rainfall records to duration. *International Journal of Climatology*, 24, 533–546. Available from: https://doi.org/10.1002/joc.1022

Gao, C., Xu, Y.-P., Zhu, Q., Bai, Z. & Liu, L. (2018) Stochastic generation of daily rainfall events: a single-site rainfall model with Copula-based joint simulation of rainfall characteristics and classification and simulation of rainfall patterns. *Journal of Hydrology*, 564, 41–58. Available from: https://doi.org/10.1016/j.jhydrol.2018.06.073

Garcia-Marin, A.P., Ayuso-Munoz, J.L., Jimenez-Hornero, F.J. & Estevez, J. (2013) Selecting the best IDF model by using the multifractal approach. *Hydrological Processes*, 27, 433–443. Available from: https://doi.org/10.1002/hyp.9272

Gaume, E., Mouhous, N. & Andrieu, H. (2007) Rainfall stochastic disaggregation models: calibration and validation of a multiplicative cascade model. *Advances in Water Resources*, 30, 1301–1319. Available from: https://doi.org/10.1016/j.advwatres.2006.11.007

Ghanmi, H., Bargaoui, Z. & Mallet, C. (2013) Investigation of the fractal dimension of rainfall occurrence in a semi-arid Mediterranean climate. *Hydrological Sciences Journal*, 58, 483–497. Available from: https://doi.org/10.1080/02626667.2013.775446

Gonzalez, S. & Bech, J. (2017) Extreme point rainfall temporal scaling: a long term (1805–2014) regional and seasonal analysis in Spain. *International Journal of Climatology*, 37, 5068–5079. Available from: https://doi.org/10.1002/joc.5144

Gutiérrez, J.M., Maraun, D., Widmann, M., Huth, R., Hertig, E., Benestad, R. et al. (2019) An intercomparison of a large ensemble of statistical downscaling methods over Europe: results from the VALUE perfect predictor cross-validation experiment. *International Journal of Climatology*, 39, 3750–3785. Available from: https://doi.org/10.1002/joc.5462

Hardwick-Jones, R., Westra, S. & Sharma, A. (2010) Relationships between extreme sub-daily precipitation, surface temperature, and relative humidity. *Geophysical Research Letters*, 37, L22805. Available from: https://doi.org/10.1029/2010GL045081

Hu, Y. & Fu, Q. (2007) Observed poleward expansion of the Hadley circulation since 1979. *Atmospheric Chemistry and Physics*, 7, 5229–5236. Available from: https://doi.org/10.5194/acp-7-5229-2007

Huang, C.C. (2011) Gaussian-distribution-based hyetographs and their relationships with debris flow initiation. *Journal of Hydrology*, 411, 251–265. Available from: https://doi.org/10.1016/j.jhydrol.2011.10.003

Huff, F.A. (1967) Time distribution of rainfall in heavy storms. *Water Resources Research*, 3, 1007–1019. Available from: https://doi.org/10.1029/WR003i004p01007

Iversen, T., Bentsen, M., Bethke, I., Debernard, J.B., Kirkevåg, A., Seland, Ø. et al. (2012) The Norwegian earth system model, NorESM1-M – part 2: climate response and scenario projections. *Geoscientific Model Development Discussion*, 5, 2933–2998. Available from: https://doi.org/10.5194/gmdd-5-2933-2012

Jacob, D., Petersen, J., Eggert, B., Alias, A., Christensen, O.B., Bouwer, L.M. et al. (2014) EURO-CORDEX: new high-resolution climate change projections for European impact research. *Regional Environmental Change*, 14, 563–578. Available from: https://doi.org/10.1007/s10113-013-0499-2

Li, X., Meshgi, A., Wang, X., Zhang, J., Tay, S.H.X., Pijcke, G. et al. (2018) Three resampling approaches based on method of fragments for daily-to-subdaily precipitation disaggregation. *International Journal of Climatology*, 38, e1119–e1138. Available from: https://doi.org/10.1002/joc.5438

Llasat, M.C. (2001) An objective classification of rainfall events on the basis of their convective features: application to rainfall intensity in the northeast of Spain. *International Journal of Climatology*, 21, 1385–1400. Available from: https://doi.org/10.1002/joc.692

Llasat, M.C. & Puigcerver, M. (1997) Total rainfall and convective rainfall in Catalonia, Spain. *International Journal of Climatology*, 17, 1683–1695. Available from: https://doi.org/10.1002/(SICI)1097-0088(199712)17:15<1683::AID-JOC220>3.0.CO;2-Q

Mandelbrot, B. (1974) Intermittent turbulence in self-similar cascades – divergence of high moments and dimension of carrier. *Journal of Fluid Mechanics*, 62, 331–358. Available from: https://doi.org/10.1017/S0022112074000711

Marsland, S.J., Haak, H., Jungclaus, J.H., Latif, M. & Roeske, F. (2003) The Max-Planck-Institute global ocean/sea ice model with orthogonal curvilinear coordinates. *Ocean Model*, 5, 91–127. Available from: https://doi.org/10.1016/S1463-5003(02)00015-X

Martin-Vide, J. & Lopez-Bustins, J.-A. (2006) The Western Mediterranean Oscillation and rainfall in the Iberian Peninsula.

International Journal of Climatology, 26, 1455–1475. Available from: https://doi.org/10.1002/joc.1388

Masugi, M. & Takuma, T. (2007) Multi-fractal analysis of IP-network traffic for assessing time variations in scaling properties. *Physica D: Nonlinear Phenomena*, 225, 119–126. Available from: https://doi.org/10.1016/j.physd.2006.10.015

Meredith, E.P., Ulbrich, U. & Rust, H.W. (2019) The diurnal nature of future extreme precipitation intensification. *Geophysical Research Letters*, 46, 7680–7689. Available from: https://doi.org/10.1029/2019GL082385

Meseguer-Ruiz, Ó., Osborn, T.J., Sarricolea, P., Jones, P.D., Olcina-Cantos, J., Serrano-Notivoli, R. et al. (2019) Definition of a temporal distribution index for high temporal resolution precipitation data over Peninsular Spain and the Balearic Islands: the fractal dimension, and its synoptic implications. *Climate Dynamics*, 52, 439–456. Available from: https://doi.org/10.1007/s00382-018-4159-6

Metzler, R. & Klafter, J. (2000) The random walk's guide to anomalous diffusion: a fractional dynamics approach. *Physics Reports*, 339, 1–77. Available from: https://doi.org/10.1016/s0370-1573(00)00070-3

Mishra, S.K., Singh, V.P. & Singh, P.K. (2018) Revisiting the soil conservation service curve number method. In: Singh, V., Yadav, S. & Yadava, R. (Eds.) *Hydrologic modeling. Water Science and Technology Library*, Vol. 81. Singapore: Springer. Available from: https://doi.org/10.1007/978-981-10-5801-1_46

Moncho, R., Belda, F. & Caselles, V. (2009) Climatic study of the exponent "n" in IDF curves: application for the Iberian Peninsula. *Tethys*, 6, 3–14. Available from: https://doi.org/10.3369/tethys.2009.6.01

Moncho, R., Belda, F. & Caselles, V. (2011) Distribución probabilística de los extremos globales de precipitación. *Nimbus*, 27–28, 119–135.

Monjo, R. (2016) Measure of rainfall time structure using the dimensionless n-index. *Climate Research*, 67, 71–86. Available from: https://doi.org/10.3354/cr01359

Monjo, R., Caselles, V. & Chust, G. (2014) Probabilistic correction of RCM precipitation in the Basque Country (Northern Spain). *Theoretical and Applied Climatology*, 117, 317–329. Available from: https://doi.org/10.1007/s00704-013-1008-8

Monjo, R., Gaitán, E., Pórtoles, J., Ribalaygua, J. & Torres, L. (2016) Changes in extreme precipitation over Spain using statistical downscaling of CMIP5 projections. *International Journal of Climatology*, 36, 757–769. Available from: https://doi.org/10.1002/joc.4380

Monjo, R. & Martin-Vide, J. (2016) Daily precipitation concentration around the world according to several indices. *International Journal of Climatology*, 36, 3828–3838. Available from: https://doi.org/10.1002/joc.4596

Monjo, R., Paradinas, C., Pórtoles, J., Gaitán, E., Redolat, D., Prado-López, C. et al. (2020) RESCCUE (RESilience to cope with Climate Change in Urban arEas) EU project – WP1 data (version 1.0) [Data Set], *Zenodo*. https://doi.org/10.5281/zenodo.3688402

Monjo, R., Pórtoles J., Gaitán E., Redolat D., Paradinas C., Prado C., et al. (2019): *Deliverable D1.3. Report on extreme events prediction. RESCCUE project. REF: Ares(2019)7770616.* https://toolkit.resccue.eu/wp-content/uploads/2020/12/d1.3_report_

on_extreme_events_prediction.pdf [Accessed 1st January 2023].

Monjo, R., Pórtoles, J. & Ribalaygua, J. (2013) Detection of inhomogeneities in daily data: a test based in the Kolmogorov-Smirnov goodness-of-fit test. *Proceedings of the 9th data management workshop of EUMETNET*, El Escorial (Madrid), 6th–8th November. https://doi.org/10.5281/zenodo.5089754

Monjo, R., Royé, D. & Martin-Vide, J. (2020) Meteorological drought lacunarity around the world and its classification. *Earth System Science Data*, 12, 741–752. Available from: https://doi.org/10.5194/essd-12-741-2020

Morbidelli, R., García-Marín, A.P., Al Mamun, A., Atiqur, R.M., Ayuso-Muñoz, J.L., Taouti, M.B. et al. (2020) The history of rainfall data time-resolution in a wide variety of geographical areas. *Journal of Hydrology*, 590, 125258. Available from: https://doi.org/10.1016/j.jhydrol.2020.125258

Müller-Thomy, H. (2020) Temporal rainfall disaggregation using a micro-canonical cascade model: Possibilities to improve the autocorrelation. *Hydrology and Earth System Sciences*, 24, 169–188. Available from: https://doi.org/10.5194/hess-24-169-2020

Na, W. & Yoo, C. (2018) Evaluation of rainfall temporal distribution models with annual maximum rainfall events in Seoul Korea. *Water*, 10, 1468. Available from: https://doi.org/10.3390/w10101468

Nguyen, V.T.V., Nguyen, T.D. & Cung, A. (2007) A statistical approach to downscaling of subdaily extreme rainfall processes for climate-related impact studies in urban areas. *Water Science and Technology: Water Supply*, 7, 183–192. Available from: https://doi.org/10.2166/ws.2007.053

Peleg, N., Fatichi, S., Paschalis, A., Molnar, P. & Burlando, P. (2017) An advanced stochastic weather generator for simulating 2-D high resolution climate variables. *Journal of Advances in Modeling Earth Systems*, 9, 1595–1627. Available from: https://doi.org/10.1002/2016MS000854

Puigcerver, M., Alonso, S., Lorente, J., Llasat, M.C., Redaño, A., Burgueño, A. et al. (1986) Preliminary aspects of rainfall rates in the north east of Spain. *Theoretical and Applied Climatology*, 37, 97–109. Available from: https://doi.org/10.1007/BF00866109

Rafatnejad, A., Tavakolifar, H. & Nazif, S. (2022) Evaluation of the climate change impact on the extreme rainfall amounts using modified method of fragments for sub-daily rainfall disaggregation. *International Journal of Climatology*, 42, 908–927. Available from: https://doi.org/10.1002/joc.7280

Rayner, D., Achberger, C. & Chen, D. (2016) A multi-state weather generator for daily precipitation for the Torne River basin, northern Sweden/western Finland. *Advances in Climate Change Research*, 7, 70–81. Available from: https://doi.org/10.1016/j.accre.2016.06.006-

Ribalaygua, J., Torres, L., Pórtoles, J., Monjo, R., Gaitán, E. & Pino, M.R. (2013) Description and validation of a two-step analogue/regression downscaling method. *Theoretical and Applied Climatology*, 114, 253–269. Available from: https://doi.org/10.1007/s00704-013-0836-x

Rodríguez, R., Casas, M. & Redaño, A. (2013) Multifractal analysis of the rainfall time distribution on the metropolitan area of Barcelona (Spain). *Meteorology and Atmospheric Physics*, 121, 181–187. Available from: https://doi.org/10.1007/s00703-013-0256-6

Rodríguez, R., Navarro, X., Casas, M.C., Ribalaygua, J., Russo, B., Pouget, L. et al. (2014) Influence of climate change on IDF curves for the metropolitan area of Barcelona (Spain). *International Journal of Climatology*, 34, 643–654. Available from: https://doi.org/10.1002/joc.3712

Rodríguez-Solà, R., Casas-Castillo, M.C., Navarro, J. & Redaño, A. (2017) A study of the scaling properties of rainfall in Spain and its appropriateness to generate intensity-duration-frequency curves from daily records. *International Journal of Climatology*, 37, 770–780. Available from: https://doi.org/10.1002/joc.4738

Schertzer, D. & Lovejoy, S. (1987) Physical modeling and analysis of rain and clouds by anisotropic scaling multiplicative processes. *Journal of Geophysical Research*, 92, 9693–9714. Available from: https://doi.org/10.1002/9781118782071.ch16

Schmitt, F.G. & Huang, Y. (2016) *Stochastic analysis of scaling time series: from turbulence theory to applications.* Cambridge, England: Cambridge University Press. Available from: https://doi.org/10.1017/CBO9781107705548

Sherman, C. (1931) Frequency and intensity of excessive rainfall at Boston, Massachusetts. *Transactions, American Society of Civil Engineers*, 95, 951–960.

Sun, X. & Barros, A.P. (2010) An evaluation of the statistics of rainfall extremes in rain gauge observations, and satellite-based and reanalysis products using universal multifractals. *Journal of Hydrometeorology*, 11, 388–404. Available from: https://doi.org/10.1175/2009JHM1142.1

Velasco, M., Russo, B., Martínez, M., Malgrat, P., Monjo, R., Djordjevic, S. et al. (2018) Resilience to cope with climate change in urban areas—a multisectoral approach focusing on water—the RESCCUE project. *Water*, 10, 1356–1366. Available from: https://doi.org/10.3390/w10101356

Voldoire, A., Sanchez-Gomez, E., Salas y Mélia, D., Decharme, B., Cassou, C., Sénési, S. et al. (2013) The CNRM-CM5.1 global climate model: description and basic evaluation. *Climate Dynamics*, 40, 2091–2121. Available from: https://doi.org/10.1007/s00382-011-1259-y

Watanabe, S., Hajima, T., Sudo, K., Nagashima, T., Takemura, T., Okajima, H. et al. (2011) MIROC-ESM 2010: model description and basic results of CMIP5-20c3m experiments. *Geoscientific Model Development*, 4, 845–872. Available from: https://doi.org/10.5194/gmd-4-845-2011

Westra, S., Alexander, L.V. & Zwiers, F.W. (2013) Global increasing trends in annual maximum daily precipitation. *Journal of Climate*, 26, 3904–3918. Available from: https://doi.org/10.1175/jcli-d-12-00502.1

Wilcox, C., Aly, C., Vischel, T., Panthou, G., Blanchet, J., Quantin, G. et al. (2021) Stochastorm: a stochastic rainfall simulator for convective storms. *Journal of Hydrometeorology*, 22, 387–404. Available from: https://doi.org/10.1175/JHM-D-20-0017.1

Xiao-Ge, X., Tong-Wen, W. & Jie, Z. (2013) Introduction of CMIP5 experiments carried out with the climate system models of Beijing climate center. *Advances in Climate Change Research*, 4, 41–49. Available from: https://doi.org/10.3724/SP.J.1248.2013.041

Yang, H., Lohmann, G., Lu, J., Gowan, E.J., Shi, X., Liu, J. et al. (2020) Tropical expansion driven by poleward advancing midlatitude meridional temperature gradients. *Journal of Geophysical Research: Atmospheres*, 125, e2020JD033158. Available from: https://doi.org/10.1029/2020JD033158

Yeo, M.-H., Nguyen, V.-T. & Kpodonu, T.A. (2021) Characterizing extreme rainfalls and constructing confidence intervals for IDF curves using Scaling-GEV distribution model. *International Journal of Climatology*, 41, 456–468. Available from: https://doi.org/10.1002/joc.6631

Yu, P.S., Yang, T.C. & Lin, C.S. (2004) Regional rainfall intensity formulas based on scaling property of rainfall. *Journal of Hydrology*, 295, 108–123. Available from: https://doi.org/10.1016/j.jhydrol.2004.03.003

Yukimoto, S., Yoshimura, H., Hosaka, M., Sakami, T., Tsujino, H., Hirabara, M. et al. (2011) Meteorological Research Institute-Earth System Model Version 1 (MRI-ESM1) – model description. Technical Report of MRI, No. 64, 83 pp.

Zhang, L., Li, H., Liu, D., Fu, Q., Li, M., Faiz, M.A. et al. (2021) Application of an improved multifractal detrended fluctuation analysis approach for estimation of the complexity of daily precipitation. *International Journal of Climatology*, 41, 4653–4671. Available from: https://doi.org/10.1002/joc.7092

Zorita, E., & von Storch, H. (1999) The analog method as a simple statistical downscaling technique: comparison with more complicated methods. *Journal of Climate*, 12, 2474–2489.

APPENDIX A: MONOFRACTAL DIMENSION OF RAINFALL INTENSITY

This appendix shows that the scaling exponent of the rainfall intensity is approximately equals to the monofractal Rényi dimension:

Let $t < t_0$ be a time given to scale a real (one-dimension) random variable I, for instance *rainfall intensity*, and $\delta = t/t_0$ be the relative size of the measuring i-th time box selected from a time series partition (i.e., regular δ-lattice cover). At each i-th time box, the scaling is provided by the Lipschitz-Hölder exponent α_i, which defines the degree of *singularity* or concentration of I at i-th time box (that is the rate of approach to infinity when δ approaches to 0). Thus, given a probability p_I of measuring I, the probability measure P_I in the distribution domain for the i-th time box scales as (Masugi & Takuma, 2007; Sun & Barros, 2010):

$$P_I(\delta) \sim p_I \delta^{-\alpha_i}, \tag{A1}$$

And also the average value

$$\langle I(t) \rangle = \sum P_I(\delta) I \sim \delta^{-\alpha_i} \sum p_I I \sim \delta^{-\alpha_i} \tag{A2}$$

In general terms, the exponent $\alpha(q)$ is related to a *mass exponent* function $\tau(q)$ by

$$\alpha(q) = \frac{d}{dq} \tau(q) \tag{A3}$$

where $q \in (-\infty, \infty)$ is the raw q-moment. Moreover, the number of boxes whose Lipschitz-Hölder exponent is α scales as

$$N_\alpha \sim \delta^{-f(\alpha)} \tag{A4}$$

while $f(\alpha) = q\alpha(q) - \tau(q)$ is a singularity function also known as *multifractal spectrum*, obtained by Legendre transformation of (Masugi & Takuma, 2007):

$$\tau(q) = (q-1) D_q \tag{A5}$$

with a family $\{D_q\}$ of the multifractal Rényi dimensions (e.g. D_0 is the box-counting or capacity dimension, D_1 is the entropy or dimension and D_2 is the correlation dimension). Therefore, taking $q = 0$, one can see that $f(\alpha) = -\tau(0) = D_0$ coincides with the box-counting dimension, and if the monofractal hypothesis (i.e., constant $D_q \quad D_0 \quad D_1$) is considered, it leads to:

$$\alpha(q) \approx \frac{d}{dq}((q-1)D_0) \approx D_0, \tag{A6}$$

$$f(\alpha) \approx qD_0 - (q-1)D_0 \approx D_0 \tag{A7}$$

On the other hand, the expected q-moment of the rainfall intensity is given by (Garcia-Marin et al., 2013; Zhang et al., 2021):

$$\langle I_q(t) \rangle \sim \langle I_q(t_0) \rangle \delta^{-\check{n}q} \rightarrow \langle I(t) \rangle \coloneqq \langle I_1(t) \rangle \sim \langle I_1(t_0) \rangle \delta^{-\check{n}} \tag{A8}$$

Finally, taking $q = 1$ in Equation (A8) and equalizing to Equations (A2) and (A6), the monofractal dimension ($\check{n}$) of the rainfall intensity is approximately equal to Lipschitz-Hölder exponent (α), and also to the monofractal Rényi dimensions (i.e., when box-counting dimension, information-entropy dimension and correlation dimension coincide).